Understanding Southern Ocean cloud controlling factors on daily time scales and their

connections to midlatitude weather systems

Mitchell Kay Kelleher

Charlottesville, Virginia

B.S. Meteorology, The University of Oklahoma, 2016

A Thesis presented to the Graduate Faculty of the University of Virginia in Candidacy for the

Degree of Master of Science

Department of Environmental Sciences

University of Virginia

February, 2018

Acknowledgments

Table of Contents

Abstract

  Clouds and their associated radiative effects are a large source of uncertainty in global climate models. Understanding of these processes is thus important to constraining model equilibrium climate sensitivity and improving future climate projections. One region with particularly large model biases in shortwave cloud radiative effects (CRE) is the Southern Ocean. Previous research has shown that many dynamical "cloud controlling factors" influence shortwave CRE on monthly time scales, and that two important cloud controlling factors over the Southern Ocean are mid-tropospheric vertical velocity and estimated inversion strength (EIS). Model errors may thus arise from biases in representing cloud controlling factors (atmospheric dynamics), representing how clouds respond to those cloud controlling factors (cloud parametrizations), or some combination thereof.

  This study extends previous work by examining cloud controlling factors over the Southern Ocean on daily time scales in both observations and global climate models. This allows the cloud controlling factors to be examined in the context of transient weather systems. Composites of EIS and mid-tropospheric vertical velocity are constructed around extratropical cyclones and anticyclones to examine how the different dynamical cloud controlling factors influence shortwave CRE around midlatitude weather systems and to assess how models compare to observations. On average, models tend to produce a realistic cyclone and anticyclone, when compared to observations, in terms of the dynamical cloud controlling factors. The difference between observations and models instead lies in how the models' shortwave CRE responds to the dynamics. In particular, the models' shortwave CRE are too sensitive to perturbations in mid-tropospheric vertical velocity and, thus, they tend to produce clouds that are too bright in the cold frontal region of the cyclone and too dim in the center of the anticyclone.

1. Introduction

Clouds are an important component of the Earth's planetary energy budget. Clouds affect the energy budget of the Earth in two major ways. First, clouds act to reflect incoming shortwave radiation away from the Earth's surface and back into space, providing a cooling effect to the planet (-47 W m^{-2} in the global average). Second, clouds absorb longwave radiation emitted from the Earth's surface and re-emit this radiation back towards the surface as well as reducing the amount of longwave radiation emitted out to space, providing a warming effect to the planet (+26 W m^{-2} in the global average). On average, in today's climate, clouds provide a net cooling effect in the global average (-21 W m^{-2}; Hartmann 2016).

However, as the climate varies and changes, the effects of clouds on Earth's climate are not expected to be constant. Given the complexity of clouds, which are affected by both dynamic and thermodynamic factors, and the strong impact of clouds on the radiative budget, clouds represent one of the largest sources of uncertainty in projections of global climate change. It is well known that, in response to an identical change in atmospheric CO_2 concentrations, global climate models produce a factor of 2 or greater difference in the global-mean surface temperature response (equilibrium climate sensitivity; Andrews et al. 2012; Forster et al. 2013), and this large spread in warming across models is largely attributed to clouds (Boucher et al. 2013; Vial et al. 2013).

In a warming climate, the longwave (warming) effects of clouds are anticipated to increase. This is thought to be due to a robust positive longwave cloud feedback in the tropics caused by the tendency for tropical high clouds to rise in such a way as to maintain nearly the same cloud top temperature as the climate warms (fixed anvil temperature hypothesis; Zelinka & Hartmann, 2010). However, shortwave cloud feedbacks with a warming climate are varied

2

across different models and additionally vary with latitude. For instance, Myers and Norris (2016) found that, owing to the competing effects of changes in global temperature and stability on subtropical low clouds in a warming climate, there is thought to be a weak positive shortwave cloud radiative feedback that acts to warm the global climate. On the other hand, poleward of 45°, climate models project a robust increase in cloud optical depth (negative extratropical shortwave cloud radiative feedback) as the climate warms, hypothesized to be due to changes in the phase of clouds from predominantly ice-dominated (which have a lower albedo) to liquid dominated mixed phase clouds (which have a higher albedo) (Zelinka et al. 2012).

Recent studies have additionally shown that many current global climate models (GCMs) and reanalyses have large biases in shortwave cloud radiative effects (CRE) at the top of the atmosphere (TOA), including over the Southern Ocean (Trenberth and Fasullo 2010; Ceppi et al. 2012). These biases potentially limit the ability of models to project changes to the climate under future anthropogenic forcing. For example, many GCMs indicate a large negative cloud feedback over the Southern Ocean in a warming climate (Trenberth and Fasullo 2010; Zelinka et al. 2012; Ceppi et al. 2016), which some studies have suggested is overestimated due to incorrect ice-liquid partitioning in mixed-phase Southern Ocean clouds (Gordon and Klein 2014; McCoy et al. 2016; Terai et al. 2016; Tan et al. 2016). This is a particular area of disagreement in the models, as there is a 40K spread in the model glaciation temperature (the temperature at which ice and liquid are equally mixed) (McCoy et al. 2016). Southern Ocean cloud biases within GCMs have also been linked to circulation and precipitation biases in both the extratropics (Ceppi et al. 2012; Ceppi et al. 2014) and the tropics (Hwang and Frierson 2013). It is thus important to understand and accurately simulate Southern Ocean clouds in order to better represent the climate system and make future projections of Earth's climate.

One method by which to evaluate whether models are accurately representing observed cloud processes is the "cloud controlling factor" framework (see recent review by Klein et al. 2017). In this framework, observed relationships between clouds and their large-scale environment are diagnosed and compared to those in models. While the cloud controlling factor framework has been extensively applied in understanding tropical and subtropical clouds (e.g., Myers and Norris 2013, 2015, 2016; Qu et al. 2014, 2015; Seethala et al. 2015; McCoy et al. 2017; Klein et al. 2017), fewer studies have focused on the dynamic and thermodynamic factors controlling midlatitude clouds and their TOA radiative effects.

At midlatitudes, key cloud controlling factors identified by previous studies include vertical velocity (e.g., Gordon et al. 2005; Norris and Iacobellis 2005; Li et al. 2014; Grise and Medeiros 2016, hereafter GM16), lower tropospheric stability (Wood and Bretherton 2006; GM16; Naud et al. 2016; Zelinka et al. 2018), near-surface temperature advection (Norris and Iacobellis 2005; Zelinka et al. 2018), surface sensible heat fluxes (Miyamoto et al. 2018), sea surface temperature (Frey and Kay 2017), and atmospheric temperature (Tselioudis et al. 1992; Gordon and Klein 2014; Terai et al. 2016; Ceppi et al. 2016). Upward vertical velocity anomalies in the midlatitudes are associated with the increased presence of clouds with tops in the mid-to-upper troposphere (e.g., Weaver and Ramanathan 1997; Li et al. 2014), as deep rising motion within the warm sector of extratropical cyclones drives nimbostratus and high-topped convective clouds (Lau and Crane 1995, 1997; Gordon et al. 2005). Downward vertical velocity anomalies inhibit the production of clouds with tops in the mid-to-upper troposphere but have been shown to be favorable for the formation of low clouds over the midlatitude oceans (Booth et al. 2013; Govekar et al. 2014; Li et al. 2014).

Enhanced subsidence above relatively low sea surface temperatures is conducive to the development of a strong boundary layer temperature inversion, which favors the development of low-level stratocumulus clouds (e.g., Klein and Hartmann 1993). A strong boundary layer inversion is particularly effective in coupling low clouds to their surface moisture source via turbulent mixing (e.g., Bretherton and Wyant 1997; Wood 2012). Additionally, a strong boundary layer inversion is associated with a decoupling of the boundary layer from the free troposphere, inhibiting dry air entrainment from the free troposphere and promoting the maintenance of low stratocumulus clouds within the boundary layer (e.g., Wood and Bretherton 2006). Cold advection into the midlatitudes can also increase low cloud cover by enhancing turbulent fluxes from the relatively warm ocean surface into the relatively cold and dry air above (Zelinka et al. 2018; Miyamoto et al. 2018). In contrast, higher sea surface temperatures strengthen the moisture gradient between the boundary layer and the free troposphere, enhancing the effectiveness of mixing dry air into the boundary layer and consequently decreasing low cloud amount and optical depth (Frey and Kay 2017).

Finally, in the midlatitudes, there is a positive correlation between cloud temperature and cloud optical depth (Gordon and Klein 2014). This occurs for two main reasons. First, for higher temperatures, for the same increase in height from a cloud base, more water vapor is condensed, increasing the optical depth of the cloud (Betts and Harshvardhan 1987; Tselioudis et al. 1998; Gordon and Klein 2014). Second, higher temperatures change the liquid-ice partitioning in the cloud leading to more liquid drops in the warmer environment, and thus resulting in increases in cloud optical depth (Tsushima et al. 2006; McCoy et al. 2014; Ceppi et al. 2016).

The observed relationships among midlatitude clouds, their radiative properties, and cloud controlling factors are often misrepresented in GCMs. Specifically, for Southern Ocean

clouds, many models overestimate the dependence of shortwave CRE on vertical velocity (GM16), and underestimate the dependence of low cloud fraction and shortwave CRE on lower tropospheric stability (GM16; Zelinka et al. 2018). This is illustrated in Fig. 6 of GM16, reproduced here as Fig. 1. The left column of Fig. 1 shows the correlation between monthly-mean anomalies of shortwave CRE and mid-tropospheric vertical velocity (ω_{500}) for observations in the top row and two subsets of global climate models ("type I" and "type II") in the bottom two rows. When comparing observations with models, it is clear that both "type I" and "type II" models overestimate the correlation between vertical velocity and shortwave CRE in the Southern Ocean. The right column of Fig. 1 shows the correlation between monthly-mean anomalies of shortwave CRE and a measure of boundary layer stability (estimate inversion strength; EIS; see section 2b for definition of EIS). In this case, a subset of models ("type I") underestimates the observed correlation between boundary layer stability and shortwave CRE and a second set of models ("type II") more accurately represent this relationship over the Southern Ocean. "Type I" and "type II" models are broadly categorized by their shortwave CRE response to a poleward jet shift. "Type I" models are those that contain a positive warming shortwave CRE for a poleward jet shift and "type II" are those that have little or no change in shortwave CRE for a poleward jet shift (see Fig. 2 contours). These two model types can also be defined in terms of their responses to certain cloud controlling factors, with shortwave CRE anomalies being a function of both EIS and ω_{500} in "type II" models and being nearly solely a function of ω_{500} in "type I" models (Fig. 2).

This result is further shown in Fig. 2 (adapted from Fig. 4 from GM16), which composites monthly-mean anomalies of shortwave CRE over the Southern Ocean as a function of the coinciding anomalies in both EIS and ω_{500}. In this figure, the axes represent the anomalies

in EIS (y-axis) and ω_{500} (x-axis), the shading represents shortwave CRE anomalies, and the contours represent the anomalous percentage of grid points falling in a region of the phase space for periods of a poleward jet shift of 1° or more (solid contours) or for periods of an equatorward jet shift of 1° or more (dashed contours). In observations and type II models (left-most and right-most panels, respectively), it is clear that shortwave CRE on monthly time scales is a function of both anomalies in boundary layer stability and vertical velocity, while type I models (middle panel) only present anomalies in shortwave CRE as a function of vertical velocity.

While not shown in Figs. 1–2, many GCMs also fail to capture the observed dependence of Southern Ocean clouds and their radiative effects on near-surface temperature advection (Zelinka et al. 2018). Additionally, the temperature dependence of Southern Ocean cloud optical depth and shortwave CRE is also overestimated in many GCMs, which has been linked to an incorrect ice-liquid partitioning in mixed-phase Southern Ocean clouds (Gordon and Klein 2014; McCoy et al. 2016; Terai et al. 2016; Tan et al. 2016).

Apart from Norris and Iacobellis (2005), the above studies have focused on monthly or longer time scales, but the processes driving midlatitude cloud variability are primarily forced by synoptic-scale weather systems that operate on much shorter time scales. While there are different ways to understand midlatitude clouds on daily time scales, such as the "weather states" approach (e.g., Oreopoulos and Rossow 2011; Tselioudis et al. 2013), in this study, I will focus on composites about the centers of extratropical cyclones and anticyclones. The cyclone compositing methodology has been used extensively by previous studies to understand the relationships between cloud properties in an extratropical cyclone and the surrounding dynamic and thermodynamic environment (e.g., Lau and Crane 1995, 1997; Naud et al. 2006; Field and Wood 2007; Posselt et al. 2008; Naud et al. 2010; Field et al. 2011). Previous studies using the

cyclone compositing methodology have suggested that Southern Ocean cloud biases are most notable within the region dominated by extratropical cyclones, particularly in the cold-air sector of the cyclone (Bodas-Salcedo et al. 2012, 2014; Williams et al. 2013; Naud et al. 2014). However, the relationship between these cyclone composite studies (based on sub-daily or daily time scales) and the cloud controlling factor studies discussed above (based on monthly time scales) has not been explored in detail.

The purpose of this study is to extend the cloud controlling factor analysis of GM16 from monthly to daily time scales. GM16 examined the relationship among midlatitude cloud radiative effects, vertical velocity, and lower tropospheric stability on monthly time scales, and found a large fraction of GCMs ("type I") underestimated the observed relationship between shortwave CRE and lower tropospheric stability and overestimated the relationship between shortwave CRE and vertical velocity, while a separate set of models ("type II") better represented the relationship between shortwave CRE and boundary layer stability (Figs. 1–2). Here, I re-examine these relationships on daily time scales, and in the context of extratropical cyclones and anticyclones for the Southern Hemisphere (SH) midlatitudes. I will attempt to answer a few key questions. First, are the relationships between shortwave CRE anomalies and anomalies in the cloud controlling factors timescale invariant? Second, do the models accurately recreate the large-scale dynamical anomalies or the shortwave CRE anomalies that exist within midlatitude weather systems? Finally, if there are biases in shortwave CRE around weather systems, can the locations of these biases be explained by the models' sensitivity to anomalies in the cloud controlling factors?

This thesis is organized as follows. Section 2 describes the data and methods used in the study. In section 3, I will examine the connections among TOA shortwave CRE, vertical

velocity, and boundary layer stability over the Southern Ocean on daily time scales, and in section 4, I will explore these relationships in the context of extratropical cyclones and anticyclones. Section 5 contains a summary and discussion of my results and section 6 concludes with a brief discussion of future work.

2. Data and Methods

a. Data

To assess the connections between Southern Ocean CRE and its dynamical cloud controlling factors on daily time scales, two observation-based datasets are used. First, vertical velocity, temperature, surface pressure, and surface dew point temperature are obtained from the ERA-Interim reanalysis product (ECMWF 2009; Dee et al. 2011). Second, daily-mean all-sky and clear-sky TOA longwave and shortwave radiative fluxes are obtained from the CERES SYN1deg-day Version 4a product (CERES Science Team 2017; Doelling et al. 2016; Loeb et al. 2018). Both observational data sets used in this work are analyzed over the time period from 2001-2016, as 2001 marks the first full year of CERES data availability.

To assess the connections between Southern Ocean CRE and its dynamical cloud controlling factors in global climate models, output from 10 models that participated in CMIP5 (WCRP 2011; Taylor et al. 2012; see list of models in Table 1) are considered. The model data are obtained from PCMDI at Lawrence Livermore National Laboratory. This analysis is restricted to these 10 models, as only a subset of the models examined by GM16 on monthly time scales contain the necessary output to calculate CRE and the dynamical cloud controlling factors on daily time scales.

9

The AMIP runs of each model, which are 30-year-long atmosphere-only model runs in which the observed radiative forcings, sea surface temperatures (SSTs), and sea ice concentrations are prescribed over the period 1979–2008, will be the focus of this study. The first ensemble member ('r1i1p1') for the AMIP scenario will be considered for each model. Focus is centered on the AMIP runs for two reasons. First, Southern Ocean SSTs are standardized across models ensuring that inter-model variance in cloud fields is not caused by variance in the SST climatology. Second, use of the AMIP runs allows for direct comparison of these results with previous studies that examined connections between SH midlatitude CRE and synoptic-scale weather systems (e.g., Bodas-Salcedo et al. 2012, 2014).

b. Methods

Following GM16, two dynamical controlling factors on SH midlatitude CRE, 500 hPa vertical velocity (ω_{500}) and estimated inversion strength (EIS; Wood and Bretherton, 2006), are considered. EIS is defined by the following calculation:

$$EIS = LTS - \Gamma_m^{850}(z_{700} - LCL) \qquad (1),$$

where the lower tropospheric stability (LTS) is defined as the difference between the potential temperature at 700 hPa and the surface, Γ_m^{850} is the moist adiabatic lapse rate at 850 hPa, z_{700} is the height of the 700 hPa level, and LCL is the height of the lifted condensation level calculated using the method of Georgakakos and Bras (1984). While both LTS and EIS are metrics of lower tropospheric stability, EIS is more strongly correlated with low cloud amount in

midlatitude low cloud regimes (Wood and Bretherton 2006; Naud et al. 2016). For this reason, EIS is analyzed in this study.

CRE is calculated as the difference in outgoing radiation at the top of the atmosphere between clear-sky and all-sky scenes (e.g., Ramanathan et al. 1989). Shortwave CRE (and not longwave CRE) is the focus of this study, as there is a greater discrepancy between observed and modeled relationships of shortwave CRE and the two dynamical cloud controlling factors considered in this study (see also GM16). Observations and models both show a strong dependence of longwave CRE on 500 hPa vertical velocity on monthly (GM16) and daily time scales. This is shown in Fig. 3, which composites the daily anomalies of longwave CRE over the Southern Ocean (45˚S-60˚S) during austral summer (DJF) as a function of the coinciding anomalies in EIS and ω_{500} for both observations and models. Because shortwave CRE is the focus in this study, the analysis is confined to austral summer when incoming solar radiation is maximized in the SH midlatitudes.

Composites of fields about the centers of extratropical cyclones and anticyclones over the Southern Ocean are constructed as follows. First, the minimum and maximum oceanic sea level pressure (SLP) anomaly over the 45°S–60°S latitude band are located for each austral summer (DJF) day over the period 2001–2016 for the observations and 1979–2008 for the AMIP model runs. This latitude band is chosen as it is the latitude band where EIS and shortwave CRE anomalies are inversely correlated, signaling a low-cloud regime (see Fig. 1b, Fig. 6b from GM16). Next, a rectangular box (4000km x 4000km) centered on the location of each SLP minimum and maximum is constructed. Finally, the radiative and dynamical fields within this box for each daily SLP minimum and maximum are averaged to yield the composite extratropical cyclone (shown in section 4a) and anticyclone (shown in section 4b) structures,

respectively. Prior to the averaging, the seasonal cycle is removed from all radiative and dynamical fields, and data points over land are excluded from the analysis.

While simple, the method described above faithfully captures the average structures of SH extratropical weather systems, as composites of surface pressure anomalies about the centers of the cyclones and anticyclones show bull's-eyes of negative and positive pressure anomalies, respectively (not shown). Additionally, it is verified that composites constructed about the center of extratropical cyclones identified using the Hodges (1994,1995,1999) feature tracking algorithm on the 850 hPa relative vorticity field produces nearly identical dynamical structures (Fig. 4) when compared to the simpler method described above, although the simpler method tends to depict a stronger cyclone on average (not shown). Feature tracking algorithms require the movement of transient weather systems to effectively track them, and while the Southern Ocean is characterized by transient ridges (e.g., Williams et al. 2013), extratropical anticyclones may be slow moving and nearly stationary features. Consequently, feature tracking algorithms that require the movement of weather systems may not be well suited to capture all anticyclones. The decision to use the simpler method to identify extratropical cyclones over the feature tracking method is thus made to ensure that the analysis of the cyclones and anticyclones is functionally equivalent.

3. SH midlatitude cloud controlling factors on daily time scales

In this section, the relationship between SH midlatitude dynamics and shortwave CRE on daily time scales in both observations and GCMs is investigated. GM16 identified the important roles of mid-tropospheric vertical velocity (ω_{500}) and lower tropospheric stability (EIS) in controlling shortwave CRE anomalies at SH midlatitudes on monthly-mean time scales. Here,

several of their key analyses are repeated to see whether the same relationships hold on daily time scales, so that a more process-based (weather system) level of understanding of midlatitude cloud biases in GCMs can be developed.

The left column of Fig. 5 shows the correlation of daily-mean ω_{500} anomalies and shortwave CRE anomalies at each grid point over the SH oceans for both observations and CMIP5 models (as shown in Fig. 1 for monthly-mean anomalies). Here, the term *anomalies* indicates that the seasonal cycle has been removed from all fields. Removing seasonality ensures that the analysis does not merely capture each model's climatology and can instead make a statement about the relative effect anomalies of each cloud controlling factor have on clouds themselves. Additionally, in this figure and all subsequent figures, focus is on the relationships between the dynamical cloud controlling factors and shortwave CRE over the SH oceans, and thus land data points are excluded where additional controlling factors must be considered.

Consistent with the monthly-mean results of GM16, Figs. 5a and 5c show a positive correlation between ω_{500} and shortwave CRE anomalies on daily time scales over the majority of the SH oceans in both observations and models (i.e., increases in mid-tropospheric vertical velocity are associated with increased cloud reflection). Only in the marine stratocumulus regions on the eastern boundaries of the subtropical oceans are the connections between ω_{500} and shortwave CRE anomalies weak. While both observations and models display a general positive correlation throughout the SH oceans, it is important to note that the values of the correlations are greater in the CMIP5 multi-model mean when compared to observations, particularly in the extratropics. This suggests that the shortwave CRE anomalies in models on average tend to be too sensitive to changes in mid-tropospheric vertical velocity.

Figures 5b and 5d show the correlation of daily-mean EIS anomalies and shortwave CRE anomalies at each grid point over the SH oceans for observations and models, respectively. Similar results for monthly-mean time scales are shown in GM16 (cf. Fig. 6b of GM16, Fig. 1b here). In deep convective regions of the tropics, increases in EIS are associated with decreased cloud reflection (increases in shortwave CRE), presumably because increasing the boundary layer stability will inhibit the development of the deep convection that drives much of the cloud formation in these regions. Outside of the tropical deep convective regime, however, increases in EIS are associated with increased cloud reflection (decreases in shortwave CRE). The magnitudes of the negative correlations in Figs. 5b and 5d are largest in the subtropical marine stratocumulus regions (off the western coasts of the continents) and over the Southern Ocean (45˚S–60˚S) where low clouds are known to be prevalent (e.g., Bromwich et al. 2012).

The correlations between daily-mean EIS and shortwave CRE anomalies are qualitatively similar, or qualitatively timescale invariant, in both observations and the CMIP5 multi-model mean (compare Figs. 5b and 5d). However, the magnitude of the negative correlations in the low cloud regions of the subtropics and midlatitudes is weaker in models (on average) than in observations, suggesting that the shortwave CRE anomalies in models are not sensitive enough to changes in EIS in SH low cloud regimes (see also Qu et al. 2015). This may be due in part to the subset of 10 models that are used in this study (see Table 1), many of which fall into the "type I" category of Grise and Polvani (2014). Type I models systematically underestimate the observed dependence of low cloud cover on EIS, whereas type II models more realistically simulate the observed relationship (cf. Fig. 7 of GM16).

Next, to better understand the relationships between shortwave CRE and the two cloud controlling factors (ω_{500} and EIS) at SH midlatitudes (45°S–60°S), composites of the shortwave

CRE anomalies in a phase space defined by daily anomalies in ω_{500} and EIS for both observations and CMIP5 models (as shown in Fig. 4 of GM16 for monthly-mean anomalies, Fig. 2 here) are constructed. The results are shown in Fig. 6, where anomalies in EIS construct the y-axis, anomalies in ω_{500} construct the x-axis, and the shading represents the shortwave CRE anomalies. Negative shortwave CRE anomalies (blue) represent increased optical depth (brighter clouds, increased cloud reflection), and positive shortwave CRE anomalies (red) represent reduced optical depth (dimmer clouds, reduced cloud reflection). For reference, the black rectangle in the center of each panel demarcates the axis bounds of the monthly-mean phase space shown in Fig. 2. The axes of the phase space shown in Fig. 6 span a much broader range of values than that shown in Fig. 2, as the dynamical cloud controlling factors have substantially larger magnitudes on daily time scales (due to synoptic-scale weather systems) that are averaged out in the monthly mean.

The ω_{500}-EIS phase space for the CMIP5 multi-model mean is shown in Fig. 6b. Consistent with Fig. 5, the shortwave CRE anomalies in the models are more sensitive to changes in ω_{500} and less sensitive to changes in EIS when compared to observations. As noted above, many models used in this study are "type I models" (see Table 1), which systematically underestimate the dependence of SH midlatitude shortwave CRE anomalies on EIS (Fig. 2b). When comparing the model average phase space to observations (Fig. 6a), two quadrants are qualitatively similar: quadrant II ($\omega_{500}' < 0$, EIS$' > 0$) and quadrant IV ($\omega_{500}' > 0$, EIS$' < 0$), and two quadrants are qualitatively different: quadrant I ($\omega_{500}' > 0$, EIS$' > 0$) and quadrant III ($\omega_{500}' < 0$, EIS$' < 0$). While there are model biases in all four quadrants of the phase space, the model biases in quadrants I and III are quantitatively larger than those in quadrants II and IV, as shown in Fig. 6c. As the models tend to be too sensitive to changes in ω_{500}, it stands to reason that at

15

least one of the quadrants (or 'dynamical regimes') with large model biases should be present in transient weather systems, such as extratropical cyclones, that contain large anomalies in ω_{500} on daily time scales. Consistent with this, Quadrants I and III correspond to specific sectors of SH midlatitude synoptic-scale weather systems where models have biases in their representation of clouds (see section 4).

In summary, the results in this section have confirmed that many of the findings of GM16 for monthly time scales also apply to daily time scales. In particular, the shortwave CRE anomalies in GCMs are, on average, too sensitive to perturbations in large-scale vertical motion at SH midlatitudes (see also Norris and Weaver 2001) and not sensitive enough to perturbations in the strength of the boundary-layer temperature inversion. However, examining daily time scales reveals some nonlinearities in these relationships that are not apparent in the monthly-mean (compare Fig. 6 with Fig. 2). In the next section, discussion will focus on how these relationships between SH midlatitude shortwave CRE anomalies and their dynamical controlling factors are manifested in the context of midlatitude weather systems.

4. Composites of SH extratropical cyclones and anticyclones

Synoptic-scale weather systems drive the dominant dynamical variability at SH midlatitudes on daily time scales. In this section, daily relationships between the two cloud controlling factors and shortwave CRE anomalies shown in Figs. 5-6 are interpreted in the context of midlatitude weather systems. To do this, composites of anomalies in the cloud controlling factors and shortwave CRE for both extratropical cyclones and anticyclones in the SH midlatitudes (45˚S–60˚S) during austral summer (DJF) are shown. The cyclone and anticyclone composites are constructed following the methods outlined in section 2b.

16

a. Extratropical cyclones

Figures 7a and 7b show the composite of ω_{500} anomalies around a SH extratropical

cyclone for both observations and the CMIP5 multi-model mean, respectively. The pattern of

ω_{500} anomalies associated with the cyclone is qualitatively very similar in observations and

models, depicting a classic 'comma-head' shape of negative ω_{500} anomalies along the fronts and

within the warm sector where rising motion would be expected to occur as in a typical

'Norwegian' cyclone (e.g., Bjerknes 1919). These negative ω_{500} anomalies are accompanied by

a region of subsidence (positive ω_{500} anomalies) in the post-cold-frontal region in both

observations and models.

Figures 7c and 7d show the composite of EIS anomalies around a SH extratropical

cyclone for both observations and the CMIP5 multi-model mean. Again, the anomalies in

observations and models are qualitatively similar. Each exhibit a negative anomaly across much

of the cyclone (in both the frontal and post-cold-frontal regions), with the minimum anomaly

shifted equatorward of the cyclone center. The negative EIS anomaly in the post-cold frontal

region is produced primarily by greater cold anomalies in potential temperature at 700 hPa than

at the surface, whereas the negative EIS anomaly extending into the warm sector of the cyclone

is produced by warm anomalies in potential temperature at the surface with weak anomalies in

potential temperature at 700 hPa (negative LTS anomalies in both cases).

The similarity of the anomalies of the cloud controlling factors in observations and

models is further illustrated in Figs. 7e and 7f, which divide the composite cyclone into the four

dynamical regimes associated with the four quadrants of the ω_{500}-EIS phase space shown in Fig.

6. Dynamical anomalies associated with quadrant I ($\omega_{500}' > 0$, EIS$' > 0$) are shown in blue,

quadrant II ($\omega_{500}' < 0$, EIS$' > 0$) in green, quadrant III ($\omega_{500}' < 0$, EIS$' < 0$) in red, and quadrant IV ($\omega_{500}' > 0$, EIS$' < 0$) in yellow. Quadrant IV anomalies typically occur in the cold air sector of the cyclone, whereas quadrant III anomalies typically occur near the center of the cyclone, in the warm sector, and along the cold front. Additionally, quadrant II anomalies typically occur in the warm sector farther to the east of the quadrant III anomalies. Quadrant I anomalies are only present far away from the cyclone center and tend to be smaller in magnitude.

In section 3, quadrants I and III were identified as regimes where CMIP5 models are most biased in representing how SH midlatitude clouds respond to dynamical controlling factors (see Fig. 2). Quadrant III anomalies are readily apparent in the frontal region and warm sector (hereafter referred to as the frontal region) of the composite cyclone (Fig. 7, bottom, red). Thus, the results in Fig. 2 suggest that a composite of shortwave CRE anomalies around the center of a SH extratropical cyclone should demonstrate a bias in this region when comparing models and observations. This is verified in Fig. 8.

Figure 8 shows the composite of shortwave CRE anomalies around a SH extratropical cyclone for both observations and the CMIP5 multi-model mean. Both observations and models show enhanced cloud reflection (negative shortwave CRE anomalies) in the region of the cyclone with upward vertical velocity anomalies (Figs. 7a and 7b) and reduced cloud reflection (positive shortwave CRE anomalies) in the cold air sector of the cyclone. However, there are key differences between the observed and model composites (Fig. 8c). First, the reduced cloud reflection to the west of the cyclone center is generally more pronounced in the models and covers more area when compared to observations. Second, the model clouds are substantially brighter in the frontal region of the cyclone. This second bias is larger in magnitude than the

18

bias to the west of the cyclone and agrees with the expectation of a model bias in the region of the cyclone with Quadrant III anomalies (Figs. 7e and 7f, red; Quadrant III from Fig. 6).

Fig. 8c shows that the majority of the model bias is located within the frontal region of the extratropical cyclone and not within the post-cold-frontal region of the cyclone, which is in contrast to the findings of some previous studies (e.g., Bodas-Salcedo et al. 2012, 2014; Williams et al. 2013). However, this is because the analyses presented here focus on anomalies from the climatology, whereas many previous studies on Southern Ocean model cloud biases retained the climatology within their analyses. To demonstrate this difference, in Fig. 9, composites of shortwave CRE around an extratropical cyclone for a single climate model (HadGEM2-A) are constructed for both the full climatology and for the anomalies. In this figure, the top panel (a) shows the difference between the observed and modeled shortwave CRE with the climatology included (cf. panel f2 of Fig. 3 of Bodas-Salcedo et al. 2014), and the bottom panel (b) shows the same result but with the climatology removed prior to performing the analysis. With the climatology included, there is little model bias in the frontal region of the cyclone and much greater model biases in the post-cold-frontal region of the cyclone (Fig. 9a), as suggested in previous studies. However, after removing the climatology, the model bias in the post-cold-frontal region is less pronounced, and a large model bias becomes apparent in the frontal region of the cyclone (Fig. 9b). The difference between the conclusions here and those of Bodas-Salcedo et al. (2014) will be discussed further in section 5.

Because the area considered in this study stretches the entire longitudinal extent of the planet, it is reasonable to consider that there may be differences in the structure of cyclones in different geographic regions of the Southern Ocean. To assess this, cyclone composites are constructed for the three main ocean basins: the South Atlantic (70˚W-25˚E), the South Indian

(25˚E-130˚E), and the South Pacific (130˚E-70˚W). To construct these composites, daily

minimum SLP anomaly locations are binned into their respective ocean basin and averages for

each composite are done using the data from those locations for each basin. Cyclones are

generally well distributed between the three basins, though the South Pacific has generally more

cyclones, likely due to its larger geographic size. Fig. 10 shows the cyclone composites for the

dynamical cloud controlling factors within each basin for observations. While the exact values

of the dynamical cloud controlling factors vary slightly between basins, the overall structure of

the dynamics around the cyclones are quite similar (and are also quite similar to the dynamical

conditions from Fig. 7), suggesting that compositing over the entirety of the Southern Ocean is

not masking out any geographic variance in cyclone structure. The same story is true for the

observed radiative composites, shown in Fig. 11. Again, while there are some slight differences,

the overall structure of the shortwave CRE anomaly composites between the ocean basins are

quite similar to each other and to the overall average, as each contain a dipole between increased

cloud reflection and decreased cloud reflection in the regions they would be expected.

   b. Extratropical anticyclones

       While many previous studies have focused on extratropical cyclone composites to

understand model cloud biases in the SH extratropics, extratropical anticyclones also play an

important role in daily weather patterns and day-to-day cloud variability at SH midlatitudes.

Figure 12 shows the composites of ω_{500} and EIS anomalies around a SH extratropical anticyclone

for both observations and the CMIP5 multi-model mean. As for the extratropical cyclone (Fig.

7), the composites of ω_{500} and EIS anomalies around the anticyclone are qualitatively very

similar between observations and models. Both observations and models show anomalous

subsidence located to the east of the anticyclone center (Figs. 12a and 12b), anomalous rising

motion located to the west of the center, and positive EIS anomalies located around the center of

the anticyclone (Figs. 12c and 12d). The east-west dipole of subsidence and rising motion is

consistent with the eastward-moving transient ridges that characterize the Southern Ocean (see

also Williams et al. 2013).

Figures 12e and 12f divide the composite anticyclone into the four dynamical regimes

associated with the four quadrants of the ω_{500}-EIS phase space (as in Figs. 7e and 7f for the

cyclone, see quadrants in Fig. 2). Two dynamical regimes dominate the anticyclone composites:

Quadrant II anomalies ($\omega_{500}' < 0$, EIS$' > 0$) typically occur to the west of the anticyclone center,

and Quadrant I anomalies ($\omega_{500}' > 0$, EIS$' > 0$) typically occur at and to the east of the

anticyclone center. As mentioned above, based on the analysis in Fig. 6, one would expect the

model shortwave CRE anomalies to be biased in the region of the anticyclone with Quadrant I

anomalies.

To assess this, Fig. 13 shows the composite of shortwave CRE anomalies around a SH

extratropical anticyclone for both observations and the CMIP5 multi-model mean. The observed

shortwave CRE anomalies are generally weak in magnitude (Fig. 13a). A small region of

reduced cloud reflection (positive shortwave CRE anomalies) is centered just to the east of the

anticyclone center, which is surrounded by a broad region of weakly enhanced cloud reflection

(negative shortwave CRE anomalies). The CMIP5 models show anomalies with a similar spatial

pattern but much greater magnitude (Fig. 13b). In particular, the positive shortwave CRE

anomalies near the center of the anticyclone have substantially greater magnitude in the models

than in observations (Fig. 13c). This result is consistent with the expectation of a substantial

model cloud bias in the region of the anticyclone with Quadrant I anomalies (Figs. 12e and 12f,

blue; Fig. 6). Consequently, in addition to the frontal sectors of extratropical cyclones, the quiescent regions associated with extratropical anticyclones are important in understanding model biases in the day-to-day variability of cloud radiative effects at SH midlatitudes.

As with the cyclone composites, Figs. 12-13 are composites for the entire longitudinal band used in the study. Again, it is important to ensure that there are no major differences in structure between the different ocean basins. Using the same method as in the cyclone composites but for daily maximum SLP anomaly locations, anticyclone composites of the dynamical and radiative fields are constructed for each ocean basin. Fig. 14 shows the anticyclone composites for the observed dynamical cloud controlling factors. As with the cyclone composites, there is broad similarity in the structure of the anticyclone between the ocean basins in terms of the dynamics. Fig. 15 shows that, as with the cyclone composites, the observed shortwave CRE field around the anticyclone is each ocean basin is also quite consistent between basins. As with the geographic distribution of cyclones, the anticyclones are also well distributed between the basins relative to each basin's geographic size. This again suggests that averaging over the entire extent of longitudes is an effective method to understand the dynamics and radiation around a typical midlatitude weather system.

5. Summary and Discussion

In recent years, a number of studies have sought to understand the climatology and variability of clouds and their radiative effects using a "cloud controlling factor" framework in both the tropics (e.g., Norris and Iacobellis 2005; Myers and Norris 2013; Qu et al. 2014, 2015; Klein et al. 2017) and extratropics (e.g., GM16; Zelinka et al. 2018). The cloud controlling factor framework identifies large-scale dynamical properties that are associated with variability

and change in observed cloud fields, which can subsequently be used to evaluate how models represent observed cloud processes. GM16 examined two such cloud controlling factors, large-scale vertical velocity (ω at 500 hPa) and boundary-layer inversion strength (estimated inversion strength, or EIS; Wood and Bretherton 2006), that were helpful in explaining variability in midlatitude cloud fields on monthly-mean time scales. In this study, their analysis is extended to daily time scales when synoptic-scale weather systems are responsible for the dominant variability in midlatitude cloud fields, focusing exclusively on the SH midlatitudes during the summer season (DJF).

Overall, the key conclusions of GM16 were found to extend from monthly-mean to daily-mean time scales. First, in both observations and global climate models, large-scale vertical motion is associated with increased cloud reflection (decreases in shortwave CRE) (Figs. 5a and 5c), confirming the well-known relationship between ascending motion and increased cloud incidence (e.g., Li et al. 2014). Second, particularly in observations, a stronger boundary layer temperature inversion (EIS) is associated with increased cloud reflection (decreases in shortwave CRE) at SH midlatitudes (Figs. 5b and 5d). This finding is consistent with the observed relationship between increased EIS and increased low cloud cover found in both tropical and extratropical low cloud regions (Wood and Bretherton 2006; Qu et al. 2015; GM16; Klein et al. 2017; Zelinka et al. 2018).

On average, global climate models overestimate the dependence of midlatitude cloud radiative effects on vertical velocity and underestimate their dependence on EIS (Figs. 5–6). The model biases are particularly pronounced in two dynamical regimes: 1) anomalously rising motion and suppressed inversion strength ($\omega_{500}' < 0$, EIS$' < 0$) and 2) anomalously sinking motion and enhanced inversion strength ($\omega_{500}' > 0$, EIS$' > 0$). On daily time scales, these

23

regimes correspond to specific sectors of extratropical weather systems. The first regime corresponds to the frontal sector of extratropical cyclones, where model clouds are on average too bright when compared to observations (Figs. 7–8; see also Bodas-Salcedo et al. 2014). The second regime corresponds to extratropical anticyclones, where model clouds are on average too few (or too dim) when compared to observations (Figs. 12–13). Global climate models well simulate how vertical velocity and EIS vary within extratropical weather systems, suggesting that the model cloud biases result primarily from errors in how the model clouds respond to the dynamics (rather than from errors in the dynamics themselves). The over-reliance of model cloud radiative effects on vertical velocity generally exaggerates the cloud reflection in regions of ascending motion and underestimates cloud reflection in regions of descending motion (see also Norris and Weaver 2001).

Several previous studies have suggested that the predominant SH midlatitude cloud biases arise from the post-cold frontal region of extratropical cyclones (e.g., Bodas-Salcedo et al. 2012, 2014; Williams et al. 2013). This is indeed the case when the climatology is retained within composites of SH extratropical cyclones for some models (e.g., Fig. 9a). However, removing the climatology allows us to more easily assess the relationship between model clouds and their underlying dynamical cloud controlling factors. When this is done, the positive bias in shortwave CRE (too little cloud reflection) in the post-cold frontal region of the cyclone has a lesser magnitude than the negative bias (too much cloud reflection) within the frontal region of the cyclone (Fig. 8c; Fig. 9b). Models, on average, better simulate the cloud perturbations associated with the dynamical anomalies in the post-cold frontal region of the cyclone ($\omega_{500}' > 0$, $EIS' < 0$; see quadrant IV of Fig. 6) than in the frontal region of the cyclone ($\omega_{500}' < 0$, $EIS' < 0$; see quadrant III of Fig. 6).

Bodas-Salcedo et al. (2014) subsequently concluded that the model bias in the post-cold-frontal region of SH extratropical cyclones is largely responsible for the well-known climatological bias of reflected shortwave radiation at SH midlatitudes, with modeled Southern Ocean clouds on average being too dim when compared to observations (Trenberth and Fasullo 2010). In Fig. 16a, a similar result is found (cf. Fig. 4 of Bodas-Salcedo et al. 2014), showing the scatter plot of each model's climatological shortwave CRE at SH midlatitudes (45°S–60°S) during the austral summer (DJF) versus its corresponding shortwave CRE in the post-cold frontal sector of a composite extratropical cyclone during the same season. Here, to be consistent with the dynamical regimes identified in section 4, the post-cold frontal sector is defined as the area of the cyclone composite for each model where there are negative anomalies of EIS and positive anomalies of ω_{500} (Figs. 7e and 7f, yellow). This differs slightly from the definition used in Bodas-Salcedo et al. (2014), who considered the post-cold frontal region to be the western two quadrants of the cyclone composite. As in Bodas-Salcedo et al. (2014), a highly significant correlation is found between the SH midlatitude shortwave CRE climatology and the climatology in the post-cold frontal sector of a composite extratropical cyclone (r = 0.96). Defining the post-cold frontal region using the definition of Bodas-Salcedo et al. (2014), as the two western quadrants of the cyclone composite, produces a comparable correlation coefficient (r = 0.97).

In Fig. 16c, the analysis Fig. 16a is repeated, but now shows the scatter plot of each model's climatological shortwave CRE with its corresponding shortwave CRE *anomaly* (i.e., with the climatology removed) in the post-cold frontal sector of the composite cyclone. Now, the correlation is no longer statistically significant, and the relationship is much weaker (r = 0.11). This suggests that the large correlation between a model's climatological shortwave CRE and its shortwave CRE in the post-cold frontal region of cyclones (Fig. 16a) may be by

construction (as both axes on the scatter plot in Fig. 16a contain the background climatological value from each model).

In Figs. 16b and 16d, the analysis from Figs. 16a and 16c is repeated, but for the combined frontal region and warm sector of the cyclone (Figs. 7e and 7f, red). In Fig. 16b, like in Fig. 16a, with the climatology included, there is a statistically significant correlation between the model shortwave CRE climatology and the cold-frontal region shortwave CRE (r = 0.98). However, in Fig. 16d, with the climatology removed, there is still a moderate correlation present (r = 0.61) between the model cyclone shortwave CRE anomaly and the model shortwave CRE climatology. This correlation is only statistically significant at the 90% level via Students' t-test, which suggests that it could be occurring by chance. Nevertheless, the results in Fig. 16 suggest that the underlying dynamics driving the cloud biases in the frontal region of the cyclone are more strongly linked to a model's climatological biases than are the dynamics of the post-cold frontal region.

Table 2 summarizes the correlations between the model shortwave CRE climatology during DJF and the shortwave CRE in each of the four dynamical regimes identified in this study. With the climatology included, there is a statistically significant correlation between a model's shortwave CRE in each of the four dynamical regimes and its shortwave CRE climatology over the entire SH midlatitudes (45˚S-60˚S). In contrast, when the climatology is removed, two of the correlations (quadrant II and quadrant IV) are no longer significant at the 95% level, and the largest remaining correlations occur in the two most biased dynamical regimes identified in this study: the regime that occurs within the frontal sector of the cyclone (quadrant III) and the regime associated with quiescent regions (quadrant I). Note that the correlation coefficients listed in Table 2 differ from those shown in Fig. 16 as they consider the

26

dynamical regimes over all oceanic grid-points (45°S-60°S), while the correlations in Fig. 16 only consider the four dynamical regimes as they exist around each model's composite cyclone (see Fig. 7f). From these results, it is unclear whether the processes driving cloud biases in any specific dynamical regime can be linked to models' climatological biases over the Southern Ocean, but if they can, the evidence in Fig. 16 and Table 2 more strongly supports that linkage coming from the cold frontal region of extratropical cyclones rather than from the post-cold frontal region.

6. Future Work

This study only examined two cloud controlling factors on SH midlatitude cloud radiative effects, following from the work of GM16, while there any many important cloud controlling factors not considered. Additional insight into model biases may be gained by examining some of the other cloud controlling factors discussed in the Introduction, such as near-surface temperature advection (Norris and Iacobellis 2005; Zelinka et al. 2018), surface sensible heat fluxes (Miyamoto et al. 2018), and tropospheric temperature perturbations (e.g., Ceppi et al. 2016). While it has been shown that the two cloud controlling factors analyzed in this study are approximately timescale-invariant (at least between monthly and daily time scales), the same cannot be said for all cloud controlling factors. On monthly time scales, Zelinka et al. (2018) recently identified near-surface temperature advection as being more important for midlatitude low cloud variability than EIS and also found that CMIP5 models poorly simulated the dependence of low cloud cover on thermal advection. However, preliminary analyses indicate that near-surface temperature advection has a much different effect on midlatitude cloud

variability on daily time scales than it does on monthly time scales (Fig. 17), and I plan to address this topic in a subsequent study.

The top panel of Fig. 17 shows the correlation between observed anomalies of surface thermal advection and shortwave CRE on a daily time-scale for all oceanic grid points in the Southern Hemisphere. While the subtropical marine stratocumulus regions show a positive correlation (cold air advection associated with increased cloud reflection), the Southern Ocean has a weakly negative correlation throughout (warm air advection associated with increased cloud reflection), even though stratocumulus is also an important cloud type within this region. These results suggest that multiple processes exist on daily time scales that connect thermal advection to clouds. For monthly time scales, shown in the bottom panel of Fig. 17, the story changes and throughout much of the midlatitudes (as in the subtropical marine stratocumulus regions) there is a positive correlation between thermal advection and cloud reflection. This positive correlation, likely due to cold air advection driving increased sensible and latent heat fluxes from the ocean into the boundary layer which results in an increase in low cloud cover (Zelinka et al. 2018), indicates that the relationship between thermal advection and shortwave CRE is not time invariant in the midlatitudes.

One potential explanation for the variant nature of thermal advection as a cloud controlling factor could be thermal advection's connection to ω_{500} on short time scales. From quasi-geostrophic (QG) theory, warm air advection is associated with rising motion. This rising motion would thus be associated with increased cloud fraction (see Fig. 5), which would cause a negative correlation between thermal advection and shortwave CRE on daily time scales if it were the only process connecting thermal advection to cloud reflection. The top panel of Fig. 18 shows the observed correlation between anomalies of thermal advection and vertical velocity on

daily time scales, and it shows that the connection expected from QG theory is present in observations within the SH midlatitudes. In other words, there is a negative correlation between the two, suggesting that warm air advection is associated with rising motion. As with the correlations between thermal advection and shortwave CRE on monthly time scales (Fig. 17, bottom), the story changes when considering the connections between vertical velocity and thermal advection on monthly time scales. In this case, shown in the bottom panel of Fig. 18, the correlation between thermal advection and vertical motion is weaker or near zero throughout the SH midlatitudes. This further suggests that multiple processes are at work, and future work should carefully consider the timescale dependence of dynamical controlling factors on clouds and their radiative effects in order to develop a better understanding of the processes responsible for observed cloud variability and model cloud biases.

References

Andrews, T., J. M. Gregory, M. J. Webb, and K. E. Taylor, 2012: Forcing, feedbacks and climate sensitivity in CMIP5 coupled atmosphere-ocean climate models. *Geophysical Research Letters*, **39**, doi:10.1029/2012GL051607.

Betts, A. K., and Harshvardhan, 1987: Thermodynamic constraint on the cloud liquid water feedback in climate models. *Journal of Geophysical Research: Atmospheres*, **92**, 8483–8485, doi:10.1029/JD092iD07p08483.

Bjerknes, J., 1919: On the structure of moving cyclones. *Mon. Wea. Rev.*, **47**, 95–99, doi:10.1175/1520-0493(1919)47<95:OTSOMC>2.0.CO;2.

Bodas-Salcedo, A., K. D. Williams, P. R. Field, and A. P. Lock, 2012: The Surface Downwelling Solar Radiation Surplus over the Southern Ocean in the Met Office Model: The Role of Midlatitude Cyclone Clouds. *J. Climate*, **25**, 7467–7486, doi:10.1175/JCLI-D-11-00702.1.

Bodas-Salcedo, A., and Coauthors, 2014: Origins of the Solar Radiation Biases over the Southern Ocean in CFMIP2 Models. *J. Climate*, **27**, 41–56, doi:10.1175/JCLI-D-13-00169.1.

Booth, J. F., C. M. Naud, and A. D. Del Genio, 2013: Diagnosing Warm Frontal Cloud Formation in a GCM: A Novel Approach Using Conditional Subsetting. *J. Climate*, **26**, 5827–5845, doi:10.1175/JCLI-D-12-00637.1.

Boucher, O., D. Randall, P. Artaxo, C. Bretherton, G. Feingold, P. Forster, V.-M. Kerminen, Y. Kondo, H. Liao, U. Lohmann, P. Rasch, S.K. Satheesh, S. Sherwood, B. Stevens and X.Y. Zhang, 2013: Clouds and Aerosols. In: Climate Change 2013: The Physical Science Basis. Contribution of Working Group I to the Fifth Assessment Report of the Intergovernmental Panel on Climate Change [Stocker, T.F., D. Qin, G.-K. Plattner, M.

Tignor, S.K. Allen, J. Boschung, A. Nauels, Y. Xia, V. Bex and P.M. Midgley (eds.)].
Cambridge University Press, Cambridge, United Kingdom and New York, NY, USA.

Bretherton, C. S., and M. C. Wyant, 1997: Moisture Transport, Lower-Tropospheric Stability, and Decoupling of Cloud-Topped Boundary Layers. *J. Atmos. Sci.*, **54**, 148–167, doi:10.1175/1520-0469(1997)054<0148:MTLTSA>2.0.CO;2.

Bromwich, D. H., and Coauthors, 2012: Tropospheric clouds in Antarctica. *Reviews of Geophysics*, **50**, doi:10.1029/2011RG000363.

Ceppi, P., Y.-T. Hwang, D. M. W. Frierson, and D. L. Hartmann, 2012: Southern Hemisphere jet latitude biases in CMIP5 models linked to shortwave cloud forcing. *Geophys. Res. Lett.*, **39**, L19708, doi:10.1029/2012GL053115.

Ceppi, P., M. D. Zelinka, and D. L. Hartmann, 2014: The response of the Southern Hemispheric eddy-driven jet to future changes in shortwave radiation in CMIP5. *Geophys. Res. Lett.*, **41**, 3244–3250, doi:10.1002/2014GL060043.

Ceppi, P., D. L. Hartmann, and M. J. Webb, 2016: Mechanisms of the Negative Shortwave Cloud Feedback in Middle to High Latitudes. *J. Climate*, **29**, 139–157, doi:10.1175/JCLI-D-15-0327.1.

CERES Science Team, 2017: CERES_SYN1deg_Ed4A data quality summary. NASA, accessed 16 November 2017, https://ceres.larc.nasa.gov/documents/DQ_summaries/ CERES_SYN1deg_Ed4A_DQS.pdf.

Dee, D. P., and Coauthors, 2011: The ERA-Interim reanalysis: configuration and performance of the data assimilation system. *Q.J.R. Meteorol. Soc.*, **137**, 553–597, doi:10.1002/qj.828.

Doelling, D. R., M. Sun, L. T. Nguyen, M. L. Nordeen, C. O. Haney, D. F. Keyes, and P. E. Mlynczak, 2016: Advances in Geostationary-Derived Longwave Fluxes for the CERES

Synoptic (SYN1deg) Product. *J. Atmos. Oceanic Technol.*, **33**, 503–521, doi:10.1175/JTECH-D-15-0147.1.

ECMWF, 2009: ECMWF public datasets web interface: ERA Interim project. ECMWF, accessed 28 November 2017, http://apps.ecmwf.int/datasets/data/interim-full-moda.

Field, P. R., and R. Wood, 2007: Precipitation and Cloud Structure in Midlatitude Cyclones. *J. Climate*, **20**, 233–254, doi:10.1175/JCLI3998.1.

Field, P. R., A. Bodas-Salcedo, and M. E. Brooks, 2011: Using model analysis and satellite data to assess cloud and precipitation in midlatitude cyclones. *Quarterly Journal of the Royal Meteorological Society*, **137**, 1501–1515, doi:10.1002/qj.858.

Forster, P. M., T. Andrews, P. Good, J. M. Gregory, L. S. Jackson, and M. Zelinka, 2013: Evaluating adjusted forcing and model spread for historical and future scenarios in the CMIP5 generation of climate models. *Journal of Geophysical Research: Atmospheres*, **118**, 1139–1150, doi:10.1002/jgrd.50174.

Frey, W. R., and J. E. Kay, 2017: The influence of extratropical cloud phase and amount feedbacks on climate sensitivity. *Clim Dyn*, 1–20, doi:10.1007/s00382-017-3796-5.

Georgakakos, K. P., and R. L. Bras, 1984: A hydrologically useful station precipitation model: 1. Formulation. *Water Resour. Res.*, **20**, 1585–1596, doi:10.1029/WR020i011p01585.

Gordon, N. D., and S. A. Klein, 2014: Low-cloud optical depth feedback in climate models. *Journal of Geophysical Research: Atmospheres*, **119**, 6052–6065, doi:10.1002/2013JD021052.

Gordon, N. D., J. R. Norris, C. P. Weaver, and S. A. Klein, 2005: Cluster analysis of cloud regimes and characteristic dynamics of midlatitude synoptic systems in observations and a model. *Journal of Geophysical Research: Atmospheres*, **110**, doi:10.1029/2004JD005027.

Govekar, P. D., C. Jakob, and J. Catto, 2014: The relationship between clouds and dynamics in

    Southern Hemisphere extratropical cyclones in the real world and a climate model. *Journal*

    of Geophysical Research: Atmospheres, **119**, 6609–6628, doi:10.1002/2013JD020699.

Grise, K. M., S.-W. Son, and J. R. Gyakum, 2013: Intraseasonal and interannual variability in

    North American storm tracks and its relationship to equatorial Pacific variability. *Mon.*

    Wea. Rev., **141**, 3610–3625.

Grise, K. M., and L. M. Polvani, 2014: Southern Hemisphere Cloud–Dynamics Biases in CMIP5

    Models and Their Implications for Climate Projections. *J. Climate*, **27**, 6074–6092,

    doi:10.1175/JCLI-D-14-00113.1.

Grise, K. M., and B. Medeiros, 2016: Understanding the Varied Influence of Midlatitude Jet

    Position on Clouds and Cloud Radiative Effects in Observations and Global Climate

    Models. *J. Climate*, **29**, 9005–9025, doi:10.1175/JCLI-D-16-0295.1.

Hartmann, D. L., 2016: Tropical anvil clouds and climate sensitivity. *PNAS,* **113 (32),** 8897-

    8899, doi:10.1073/pnas.1610455113.

Hodges, K. I., 1994: A General Method for Tracking Analysis and Its Application to

    Meteorological Data. *Mon. Wea. Rev.*, **122**, 2573–2586, doi:10.1175/1520-

    0493(1994)122<2573:AGMFTA>2.0.CO;2.

Hodges, K. I., 1995: Feature Tracking on the Unit Sphere. *Mon. Wea. Rev.*, **123**, 3458–3465,

    doi:10.1175/1520-0493(1995)123<3458:FTOTUS>2.0.CO;2.

Hodges, K. I., 1999: Adaptive Constraints for Feature Tracking. *Mon. Wea. Rev.*, **127**, 1362–

    1373, doi:10.1175/1520-0493(1999)127<1362:ACFFT>2.0.CO;2.

Hwang, Y.-T., and D. M. W. Frierson, 2013: Link between the double-Intertropical Convergence

    Zone problem and cloud biases over the Southern Ocean. *PNAS*, **110**, 4935–4940,

    doi:10.1073/pnas.1213302110.

Klein, S. A., and D. L. Hartmann, 1993: The Seasonal Cycle of Low Stratiform Clouds. *J.*

    Climate, **6**, 1587–1606, doi:10.1175/1520-0442(1993)006<1587:TSCOLS>2.0.CO;2.

Klein S. A., A. Hall, J. R. Norris, and R. Pincus, 2017: Low-Cloud Feedbacks from Cloud-

    Controlling Factors: A Review. *Surv Geophys*, **38**, 1307–1329, doi:10.1007/s10712-017-

    9433-3.

Lau, N.-C., and M. W. Crane, 1995: A Satellite View of the Synoptic-Scale Organization of

    Cloud Properties in Midlatitude and Tropical Circulation Systems. *Mon. Wea. Rev.*, **123**,

    1984–2006, doi:10.1175/1520-0493(1995)123<1984:ASVOTS>2.0.CO;2.

Lau, N.-C., and M. W. Crane, 1997: Comparing Satellite and Surface Observations of Cloud

    Patterns in Synoptic-Scale Circulation Systems. *Mon. Wea. Rev.*, **125**, 3172–3189,

    doi:10.1175/1520-0493(1997)125<3172:CSASOO>2.0.CO;2.

Li, Y., D. W. J. Thompson, G. L. Stephens, and S. Bony, 2014: A global survey of the

    instantaneous linkages between cloud vertical structure and large-scale climate. *Journal of*

    Geophysical Research: Atmospheres, **119**, 3770–3792, doi:10.1002/2013JD020669.

Loeb, N. G., and Coauthors, 2017: Clouds and the Earth's Radiant Energy System (CERES)

    Energy Balanced and Filled (EBAF) Top-of-Atmosphere (TOA) Edition-4.0 Data Product.

    J. Climate, **31**, 895–918, doi:10.1175/JCLI-D-17-0208.1.

McCoy, D. T., D. L. Hartmann, and D. P. Grosvenor, 2014: Observed Southern Ocean Cloud

    Properties and Shortwave Reflection. Part II: Phase Changes and Low Cloud Feedback. *J.*

    Climate, **27**, 8858–8868, doi:10.1175/JCLI-D-14-00288.1.

McCoy, D. T., I. Tan, D. L. Hartmann, M. D. Zelinka, and T. Storelvmo, 2016: On the

    relationships among cloud cover, mixed-phase partitioning, and planetary albedo in GCMs.

    Journal of Advances in Modeling Earth Systems, **8**, 650–668, doi:10.1002/2015MS000589.

McCoy, D. T., R. Eastman, D. L. Hartmann, and R. Wood, 2017: The Change in Low Cloud

    Cover in a Warmed Climate Inferred from AIRS, MODIS, and ERA-Interim. *J. Climate*,

    30, 3609–3620, doi:10.1175/JCLI-D-15-0734.1.

Miyamoto, A., H. Nakamura, and T. Miyasaka, 2018: Influence of the Subtropical High and

    Storm Track on Low-Cloud Fraction and Its Seasonality over the South Indian Ocean. *J.*

    Climate, **31**, 4017–4039, doi:10.1175/JCLI-D-17-0229.1.

Myers, T., and J. Norris, 2016: Reducing the uncertainty in subtropical cloud feedback.

    Geophysical Research Letters, **43**, 2144–2148, doi:10.1002/2015GL067416.

Myers, T. A., and J. R. Norris, 2013: Observational Evidence That Enhanced Subsidence

    Reduces Subtropical Marine Boundary Layer Cloudiness. *J. Climate*, **26**, 7507–7524,

    doi:10.1175/JCLI-D-12-00736.1.

Myers, T. A., and J. R. Norris, 2015: On the Relationships between Subtropical Clouds and

    Meteorology in Observations and CMIP3 and CMIP5 Models. *J. Climate*, **28**, 2945–2967,

    doi:10.1175/JCLI-D-14-00475.1.

Naud, C. M., A. D. Del Genio, and M. Bauer, 2006: Observational Constraints on the Cloud

    Thermodynamic Phase in Midlatitude Storms. *J. Climate*, **19**, 5273–5288,

    doi:10.1175/JCLI3919.1.

Naud, C. M., A. D. Del Genio, and M. Bauer, and W. Kovari, 2010: Cloud Vertical Distribution

    across Warm and Cold Fronts in CloudSat–CALIPSO Data and a General Circulation

    Model. *J. Climate*, **23**, 3397–3415, doi:10.1175/2010JCLI3282.1.

Naud, C. M., J. F. Booth, and A. D. Del Genio, 2014: Evaluation of ERA-Interim and MERRA Cloudiness in the Southern Ocean. *J. Climate*, **27**, 2109–2124, doi:10.1175/JCLI-D-13-00432.1.

Naud, C. M., J. F. Booth, and A. D. Del Genio, 2016: The Relationship between Boundary Layer Stability and Cloud Cover in the Post-Cold-Frontal Region. *J. Climate*, **29**, 8129–8149, doi:10.1175/JCLI-D-15-0700.1.

Norris, J. R., and S. F. Iacobellis, 2005: North Pacific Cloud Feedbacks Inferred from Synoptic-Scale Dynamic and Thermodynamic Relationships. *J. Climate*, **18**, 4862–4878, doi:10.1175/JCLI3558.1.

Norris, J. R., and C. P. Weaver, 2001: Improved Techniques for Evaluating GCM Cloudiness Applied to the NCAR CCM3. *J. Climate*, **14**, 2540–2550, doi:10.1175/1520-0442(2001)014<2540:ITFEGC>2.0.CO;2.

Oreopoulos, L., and W. B. Rossow, 2011: The cloud radiative effects of International Satellite Cloud Climatology Project weather states. *Journal of Geophysical Research: Atmospheres*, **116**, doi:10.1029/2010JD015472.

Posselt, D. J., G. L. Stephens, and M. Miller, 2008: CLOUDSAT: Adding a New Dimension to a Classical View of Extratropical Cyclones. *Bull. Amer. Meteor. Soc.*, **89**, 599–610, doi:10.1175/BAMS-89-5-599.

Qu, X., A. Hall, S. A. Klein, and P. M. Caldwell, 2014: On the spread of changes in marine low cloud cover in climate model simulations of the 21st century. *Clim Dyn*, **42**, 2603–2626, doi:10.1007/s00382-013-1945-z.

Qu, X., A. Hall, S. A. Klein, and A. M. DeAngelis, 2015: Positive tropical marine low-cloud cover feedback inferred from cloud-controlling factors. *Geophys. Res. Lett.*, **42**, 2015GL065627, doi:10.1002/2015GL065627.

Ramanathan, V., R. D. Cess, E. F. Harrison, P. Minnis, B. R. Barkstrom, E. Ahmad, and D. Hartmann, 1989: Cloud-Radiative Forcing and Climate: Results from the Earth Radiation Budget Experiment. *Science*, **243**, 57–63, doi:10.1126/science.243.4887.57.

Seethala, C., J. R. Norris, and T. A. Myers, 2015: How Has Subtropical Stratocumulus and Associated Meteorology Changed since the 1980s? *J. Climate*, **28**, 8396–8410, doi:10.1175/JCLI-D-15-0120.1.

Tan, I., T. Storelvmo, and M. D. Zelinka, 2016: Observational constraints on mixed-phase clouds imply higher climate sensitivity. *Science*, **352**, 224–227, doi:10.1126/science.aad5300.

Taylor, K. E., R. J. Stouffer, and G. A. Meehl, 2012: An Overview of CMIP5 and the Experiment Design. *Bull. Amer. Meteor. Soc.*, **93**, 485–498, doi:10.1175/BAMS-D-11-00094.1.

Terai, C. R., S. A. Klein, and M. D. Zelinka, 2016: Constraining the low-cloud optical depth feedback at middle and high latitudes using satellite observations. *Journal of Geophysical Research: Atmospheres*, **121**, 9696–9716, doi:10.1002/2016JD025233.

Trenberth, K. E., and J. T. Fasullo, 2010: Simulation of Present-Day and Twenty-First-Century Energy Budgets of the Southern Oceans. *J. Climate*, **23**, 440–454, doi:10.1175/2009JCLI3152.1.

Tselioudis, G., W. B. Rossow, and D. Rind, 1992: Global Patterns of Cloud Optical Thickness Variation with Temperature. *J. Climate*, **5**, 1484–1495, doi:10.1175/1520-0442(1992)005<1484:GPOCOT>2.0.CO;2.

Tselioudis, G., A. D. DelGenio, W. Kovari, and M.-S. Yao, 1998: Temperature Dependence of Low Cloud Optical Thickness in the GISS GCM: Contributing Mechanisms and Climate Implications. *J. Climate*, **11**, 3268–3281, doi:10.1175/1520-0442(1998)011<3268:TDOLCO>2.0.CO;2.

Tselioudis, G., W. Rossow, Y. Zhang, and D. Konsta, 2013: Global Weather States and Their Properties from Passive and Active Satellite Cloud Retrievals. *J. Climate*, **26**, 7734–7746, doi:10.1175/JCLI-D-13-00024.1.

Tsushima, Y., and Coauthors, 2006: Importance of the mixed-phase cloud distribution in the control climate for assessing the response of clouds to carbon dioxide increase: a multi-model study. *Clim Dyn*, **27**, 113–126, doi:10.1007/s00382-006-0127-7.

Vial, J., J.-L. Dufresne, and S. Bony, 2013: On the interpretation of inter-model spread in CMIP5 climate sensitivity estimates. *Clim Dyn*, **41**, 3339–3362, doi:10.1007/s00382-013-1725-9.

WCRP, 2011: Coupled Model Intercomparison Project, phase 5. Earth System Grid Federation, Lawrence Livermore National Laboratory, accessed 30 March 2018, https://esgf-node.llnl.gov/search/cmip5.

Weaver, C. P., and V. Ramanathan, 1997: Relationships between Large-Scale Vertical Velocity, Static Stability, and Cloud Radiative Forcing over Northern Hemisphere Extratropical Oceans. *J. Climate*, **10**, 2871–2887, doi:10.1175/1520-0442(1997)010<2871:RBLSVV>2.0.CO;2.

Williams, K. D., and Coauthors, 2013: The Transpose-AMIP II Experiment and Its Application to the Understanding of Southern Ocean Cloud Biases in Climate Models. *J. Climate*, **26**, 3258–3274, doi:10.1175/JCLI-D-12-00429.1.

Wood, R., and C. S. Bretherton, 2006: On the Relationship between Stratiform Low Cloud Cover and Lower-Tropospheric Stability. *J. Climate*, **19**, 6425–6432, doi:10.1175/JCLI3988.1.

Wood, R., 2012: Stratocumulus Clouds. *Mon. Wea. Rev.*, **140**, 2373–2423, doi:10.1175/MWR-D-11-00121.1.

Zelinka, M. D., and D. L. Hartmann, 2010: Why is longwave cloud feedback positive? *J. Geophys. Res.*, **115**, D16117, doi:10.1029/2010JD013817.

Zelinka, M. D., S. A. Klein, and D. L. Hartmann, 2012: Computing and Partitioning Cloud Feedbacks Using Cloud Property Histograms. Part II: Attribution to Changes in Cloud Amount, Altitude, and Optical Depth. *J. Climate*, **25**, 3736–3754, doi:10.1175/JCLI-D-11-00249.1.

Zelinka, M. D., K. M. Grise, S. A. Klein, C. Zhou, A. M. DeAngelis, and M. W. Christensen, 2018: Drivers of the Low-Cloud Response to Poleward Jet Shifts in the North Pacific in Observations and Models. *J. Climate*, **31**, 7925–7947, doi:10.1175/JCLI-D-18-0114.1.

Tables and Captions

TABLE 1. Listing of the CMIP5 models used in this study. The model types reflect the

categorization of Grise and Polvani (2014).

Model name	Modeling center	Model Type
BCC_CSM1.1(m)	Beijing Climate Center, China Meteorological Administration	I
CanAM4	Canadian Centre for Climate Modelling and Analysis	I
CNRM-CM5	Centre National de Recherches Météorologiques/Centre Européen de Recherche et de Formation Avancée en Calcul Scientifique	I
GFDL-CM3	National Oceanic and Atmospheric Administration (NOAA)/GFDL	II
HadGEM2-A	Met Office Hadley Centre	II
IPSL-CM5A-LR	L'Institut Pierre-Simon Laplace	I
IPSL-CM5B-LR	L'Institut Pierre-Simon Laplace	II
MIROC5	Atmosphere and Ocean Research Institute (The University of Tokyo), National Institute for Environmental Studies, and Japan Agency for Marine-Earth Science and Technology	II
MPI-ESM-LR	Max Planck Institute for Meteorology	I
MRI-CGCM3	Meteorological Research Institute	II

TABLE 2. Correlation between model austral summer (DJF) TOA shortwave CRE climatology and model TOA shortwave CRE averaged over each dynamical regime (quadrant) over the entire Southern Hemisphere midlatitudes (45˚S–60˚S). The second column lists the correlation with the climatology included in the shortwave CRE in each dynamical regime, and the third column lists the correlation with the climatology removed from the shortwave CRE in each dynamical regime. Two asterisks indicate significance at the 95% level.

Quadrant	Correlation (Climatology)	Correlation (Anomalies)
I (Blue)	0.92**	-0.71**
II (Green)	0.93**	-0.38
III (Red)	0.97**	0.67**
IV (Yellow)	0.96**	0.49

Figures and Captions
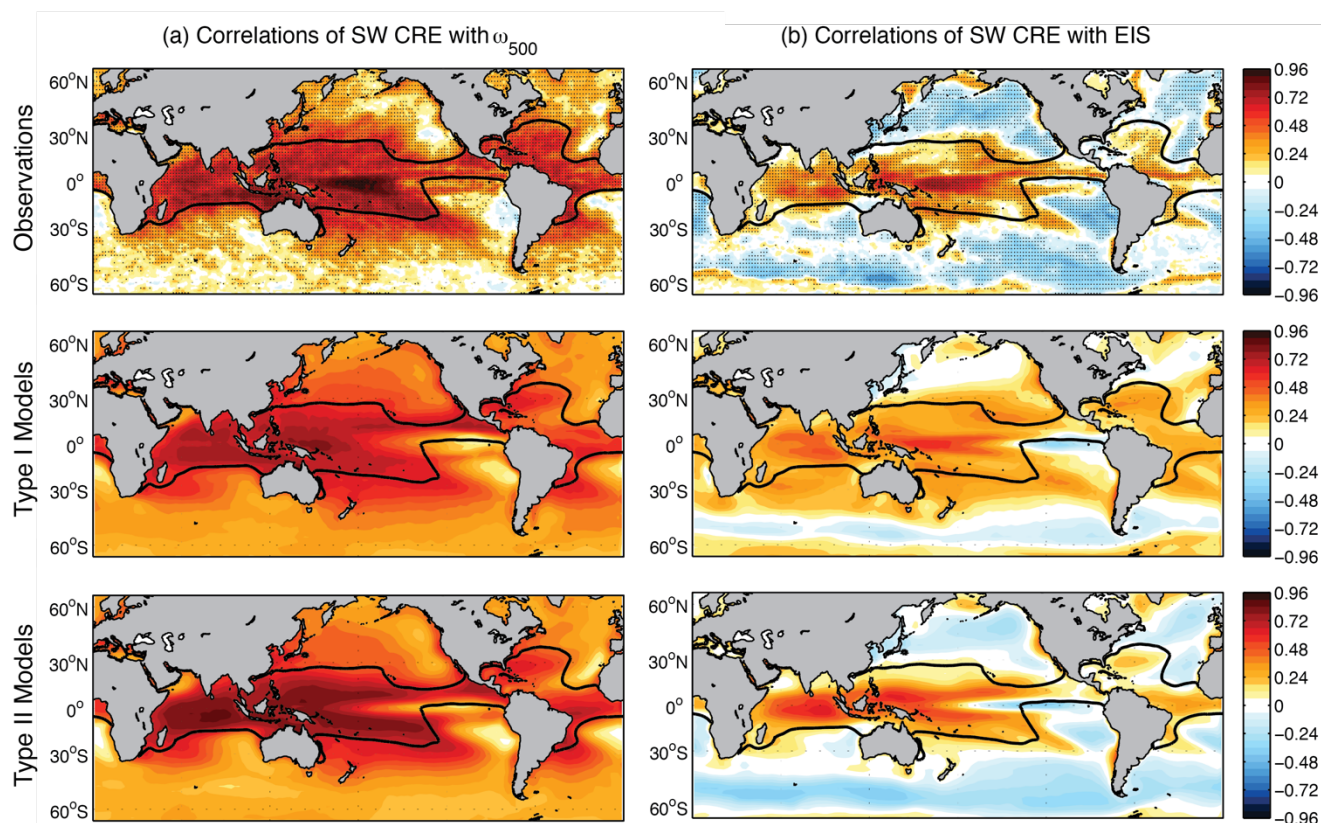
FIG. 1. Correlations between anomalies of shortwave CRE and two dynamical cloud controlling factors on monthly time scales. Column (a) shows the correlations between shortwave CRE and ω_{500}, and column (b) shows the correlations between shortwave CRE and estimated inversion strength (EIS). The first row displays the correlations in observations, and the second and third row display the correlations in type I and type II models as defined in Grise & Polvani (2014). The thin solid black line highlights where the observed long-term mean climatology of EIS exceeds 2K. Stippling in the top row indicates regions where the correlations are significant at the 95% level. Adapted from Fig. 6 from Grise & Medeiros (2016), copyright *American Meteorological Society*.
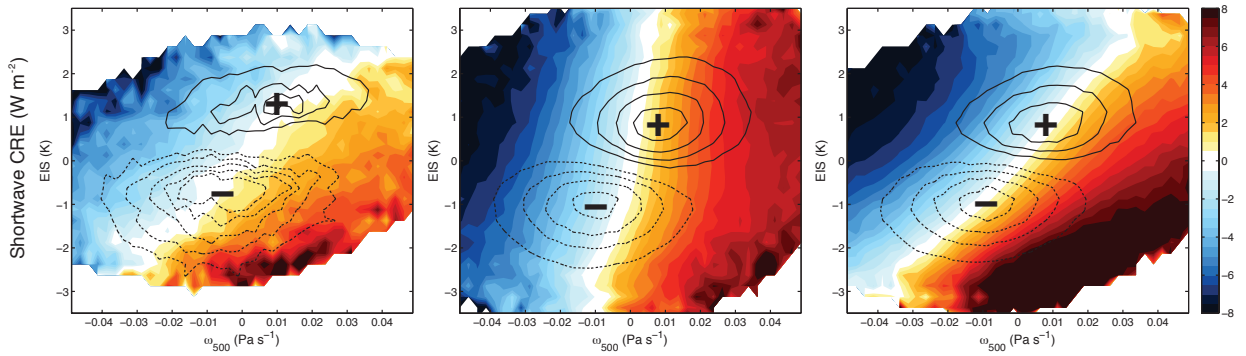
FIG. 2. Monthly anomalies in shortwave CRE composited as a function of the coinciding EIS (y-axis) and ω_{500} (x-axis) anomalies over oceanic grid points occurring between 40˚S and 50˚S. The leftmost panel shows the observations, and the middle and rightmost panels show the result from type I and type II models, respectively, as defined in Grise & Polvani (2014). The contours show the anomalous percentage of grid points falling in a region of the ω_{500}-EIS phase space for a $\geq 1˚$ latitude poleward jet shift (solid contours) or for a $\geq 1˚$ latitude equatorward jet shift (dashed contours). Adapted from Fig. 4 from Grise & Medeiros (2016) copyright *American Meteorological Society*.
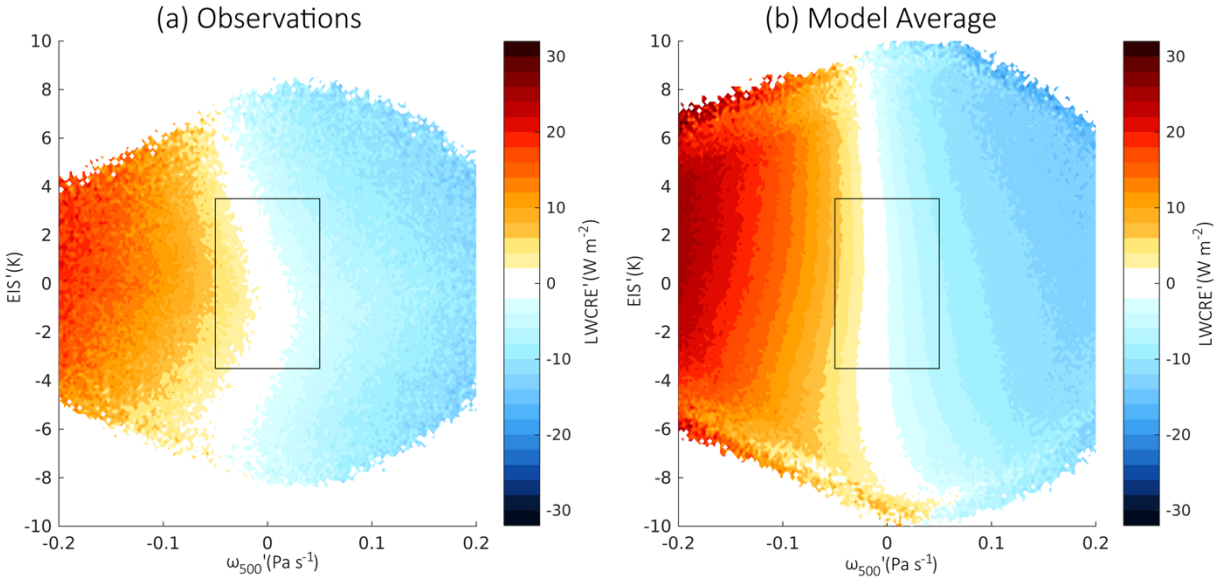
FIG. 3. Composites of daily longwave CRE (LWCRE) anomalies (W m^{-2}) over the Southern Ocean (45˚S–60˚S) during austral summer (DJF), plotted as a function of the coinciding anomalies in EIS (y-axis, K) and ω_{500} (x-axis, Pa s^{-1}). The observed composite is shown in panel a, and the average of the composites from 10 CMIP5 models is shown in panel b. The black box represents the axes bounds used in Grise and Medeiros (2016) for monthly anomalies in the cloud controlling factors.
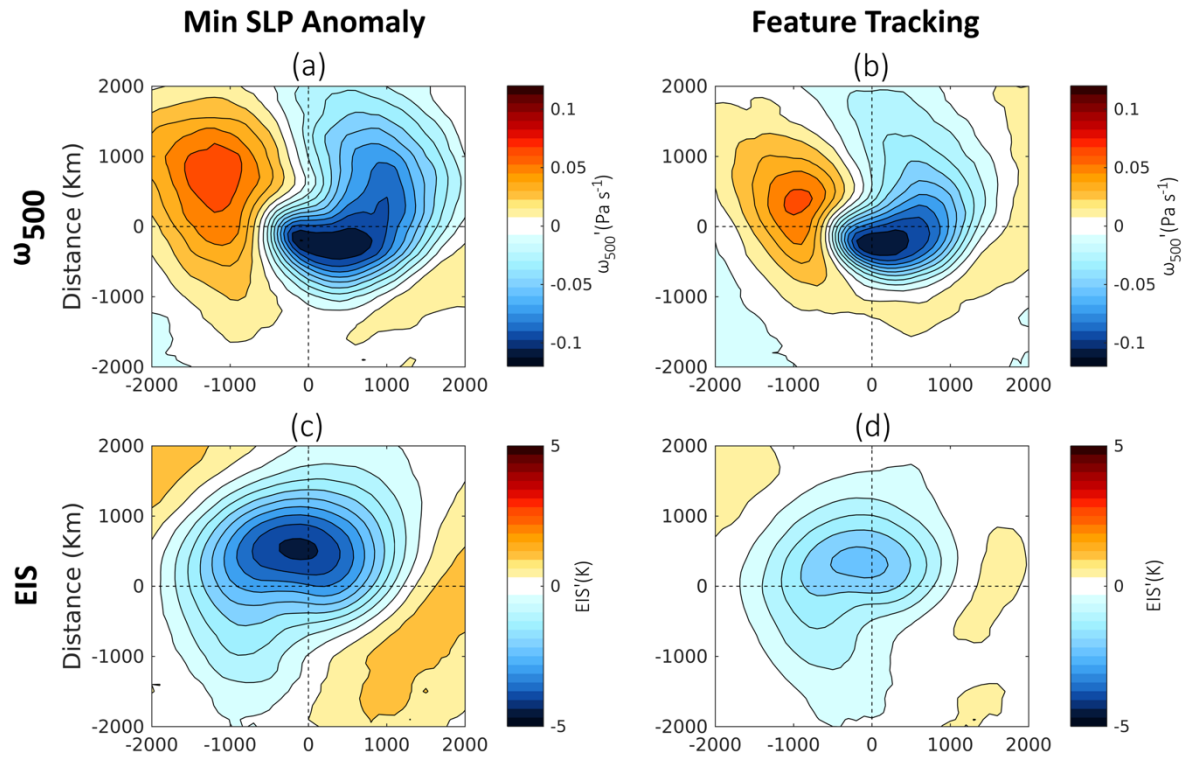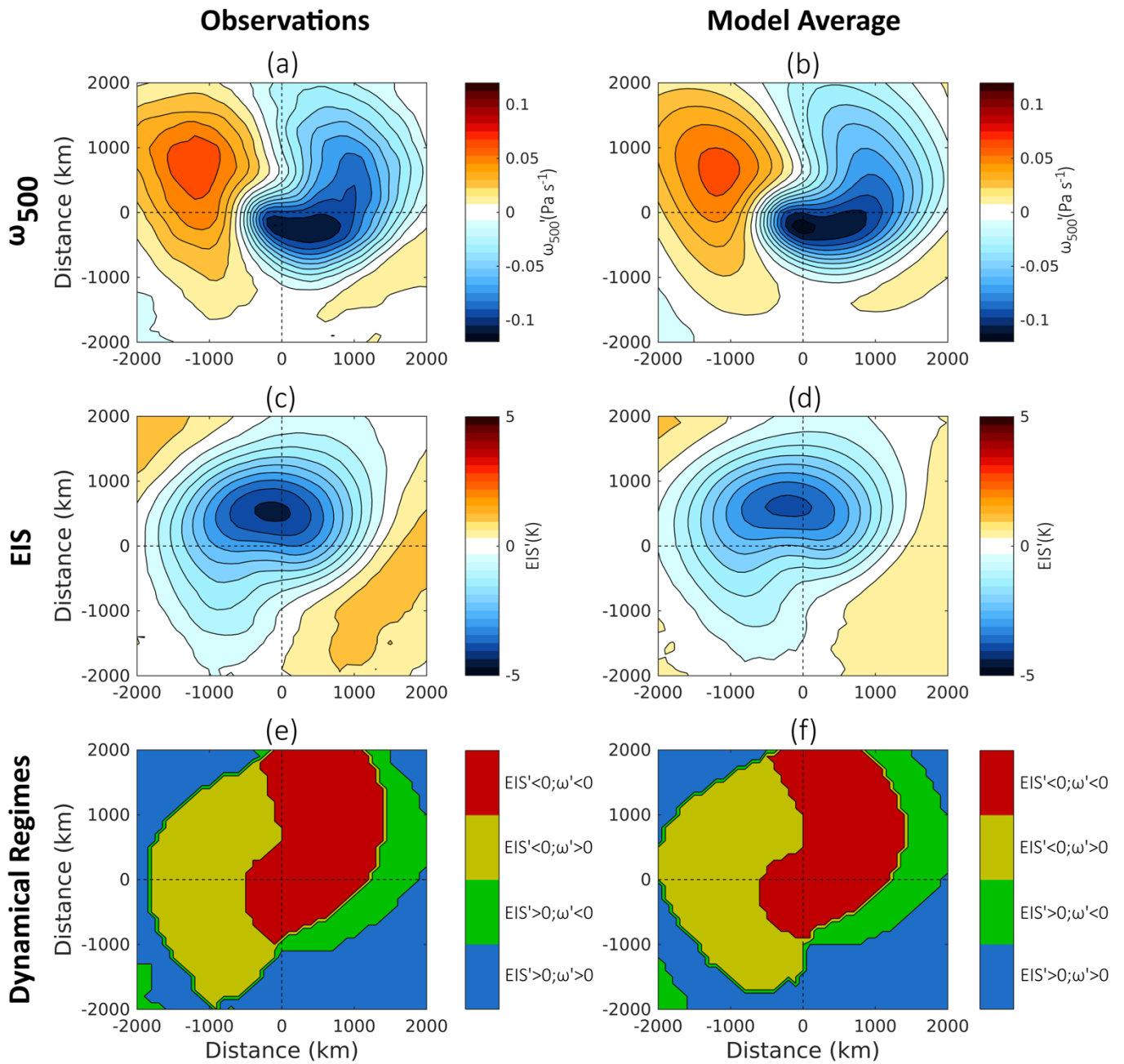
FIG. 4. Composites of daily anomalies of cloud controlling factors around the centers of extratropical cyclones over the Southern Ocean (45˚S–60˚S) during DJF from the ERA-Interim reanalysis (2001–2016). The left column represents the structure of extratropical cyclones when using daily minima in oceanic sea level pressure to identify cyclone centers. The right column depicts the structure of extratropical cyclones when using the Hodges (1994, 1995, 1999) feature tracking algorithm to identify cyclone centers. The cyclone tracking is performed following the procedure outlined in Grise et al. (2013). The top row (a, b) shows composites of ω_{500} anomalies (Pa s^{-1}), and the bottom row (c, d) shows composites of EIS anomalies (K).
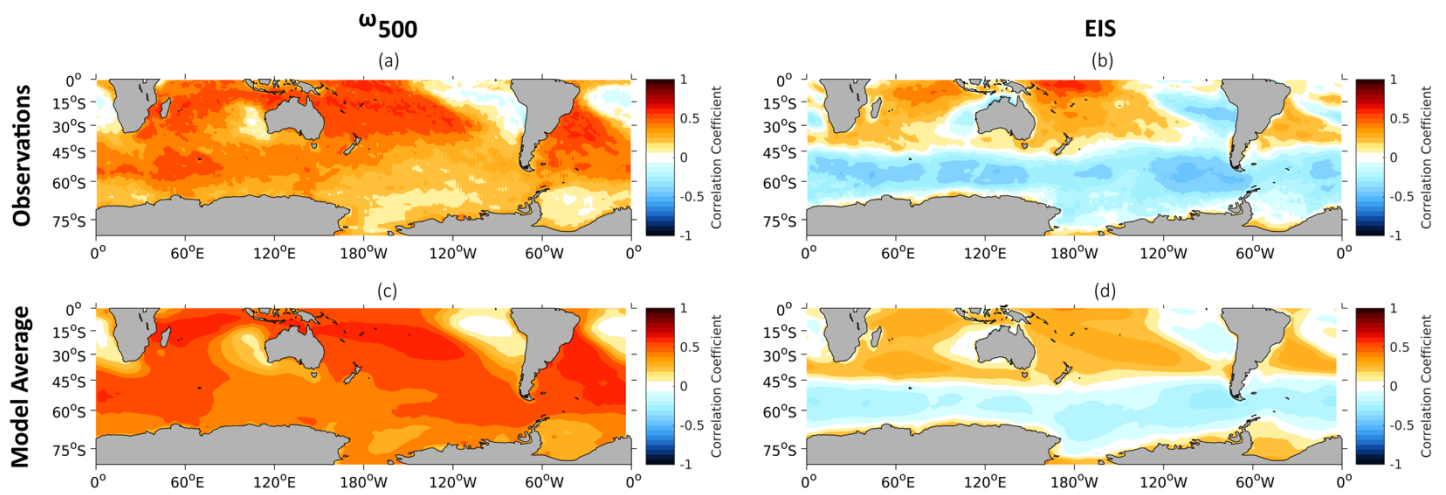
FIG. 5. Correlation coefficients between shortwave CRE anomalies and anomalies of (a, c) ω_{500} and (b, d) EIS on a daily timescale. The observed correlation coefficients are shown in the top row, and the average of correlation coefficients from 10 CMIP5 models is shown in the bottom row.
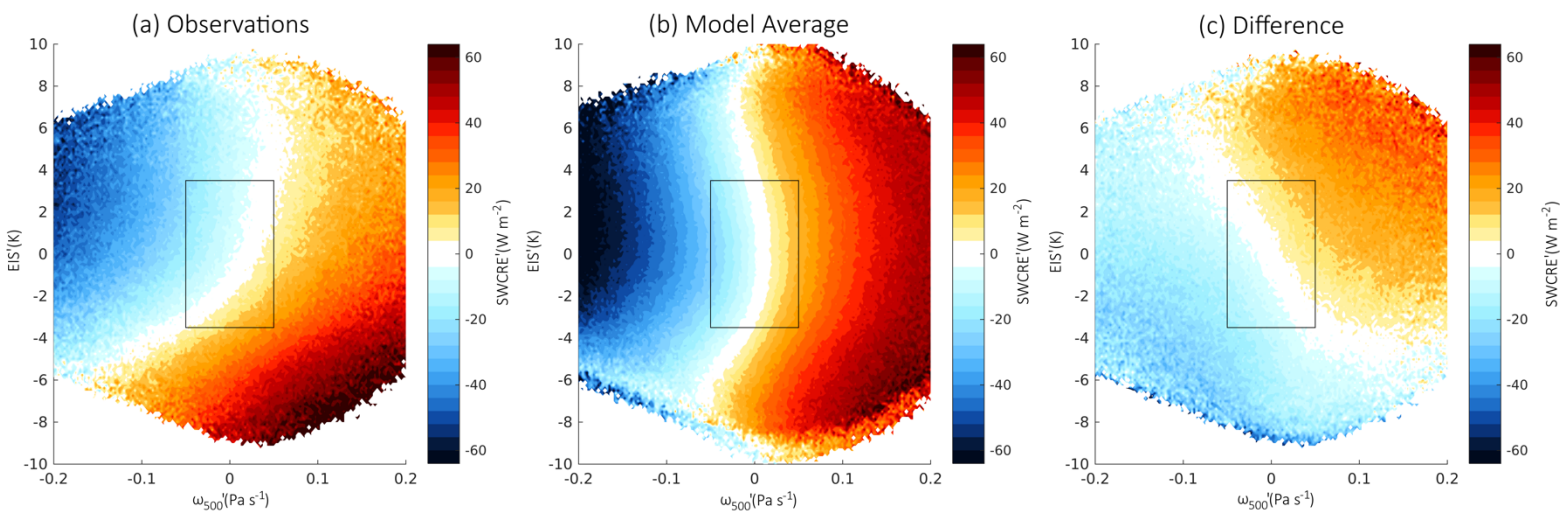
FIG. 6. Composites of daily shortwave CRE (SWCRE) anomalies (W m^{-2}) over the Southern Ocean (45˚S–60˚S) during DJF, plotted as a function of the coinciding anomalies in EIS (y-axis, K) and ω_{500} (x-axis, Pa s^{-1}). The observed composite is shown in panel a, the average of the composites from 10 CMIP5 models is shown in panel b, and the difference is shown in panel c. The black box represents the axes bounds used in GM16 for monthly anomalies in the cloud controlling factors.

FIG. 7. Composites of daily anomalies of cloud controlling factors around the centers of extratropical cyclones over the Southern Ocean (45˚S–60˚S) during DJF. Observed cyclone composites are in the left column, and the CMIP5 multi-model-mean cyclone composites are in the right column. The top row (a, b) shows composites of ω_{500} anomalies (Pa s^{-1}), the middle row (c, d) shows composites of EIS anomalies (K), and the bottom row (e, f) shows where the different dynamical regimes (quadrants of Fig. 8) are located in the context of a composite SH extratropical cyclone.
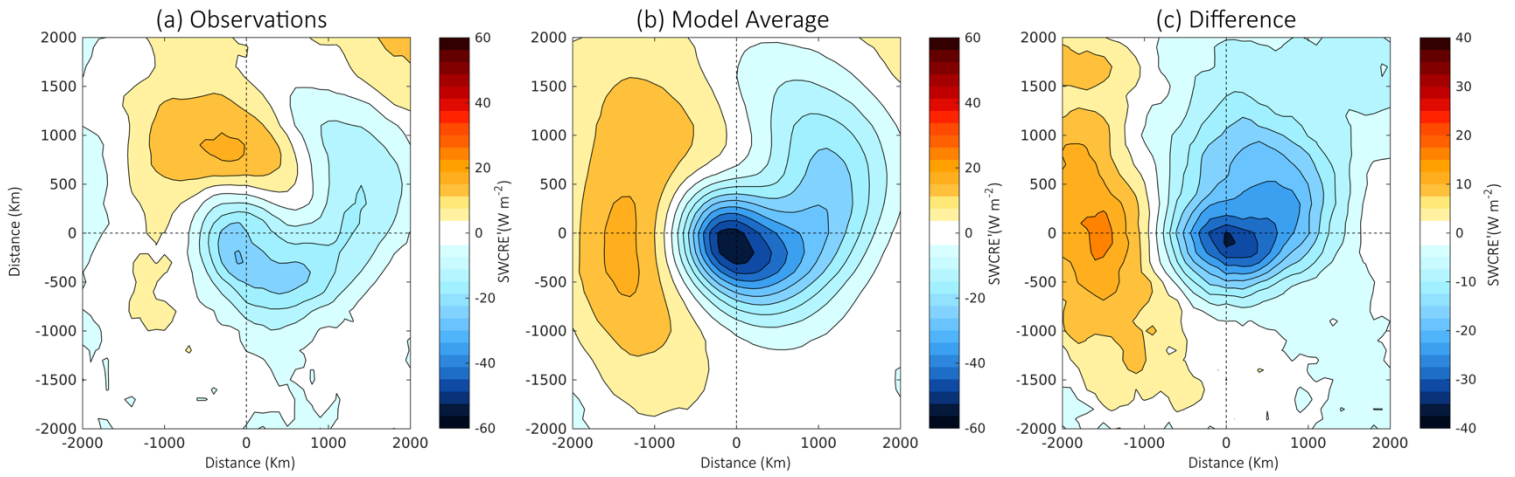
FIG. 8. Composites of daily SWCRE anomalies (W m^{-2}) around the centers of extratropical cyclones over the Southern Ocean (45˚S–60˚S) during DJF. Panel a shows the SWCRE anomalies for the observed cyclone composite, panel b shows the SWCRE anomalies for the CMIP5 multi-model-mean cyclone composite, and panel c shows the difference between the two.
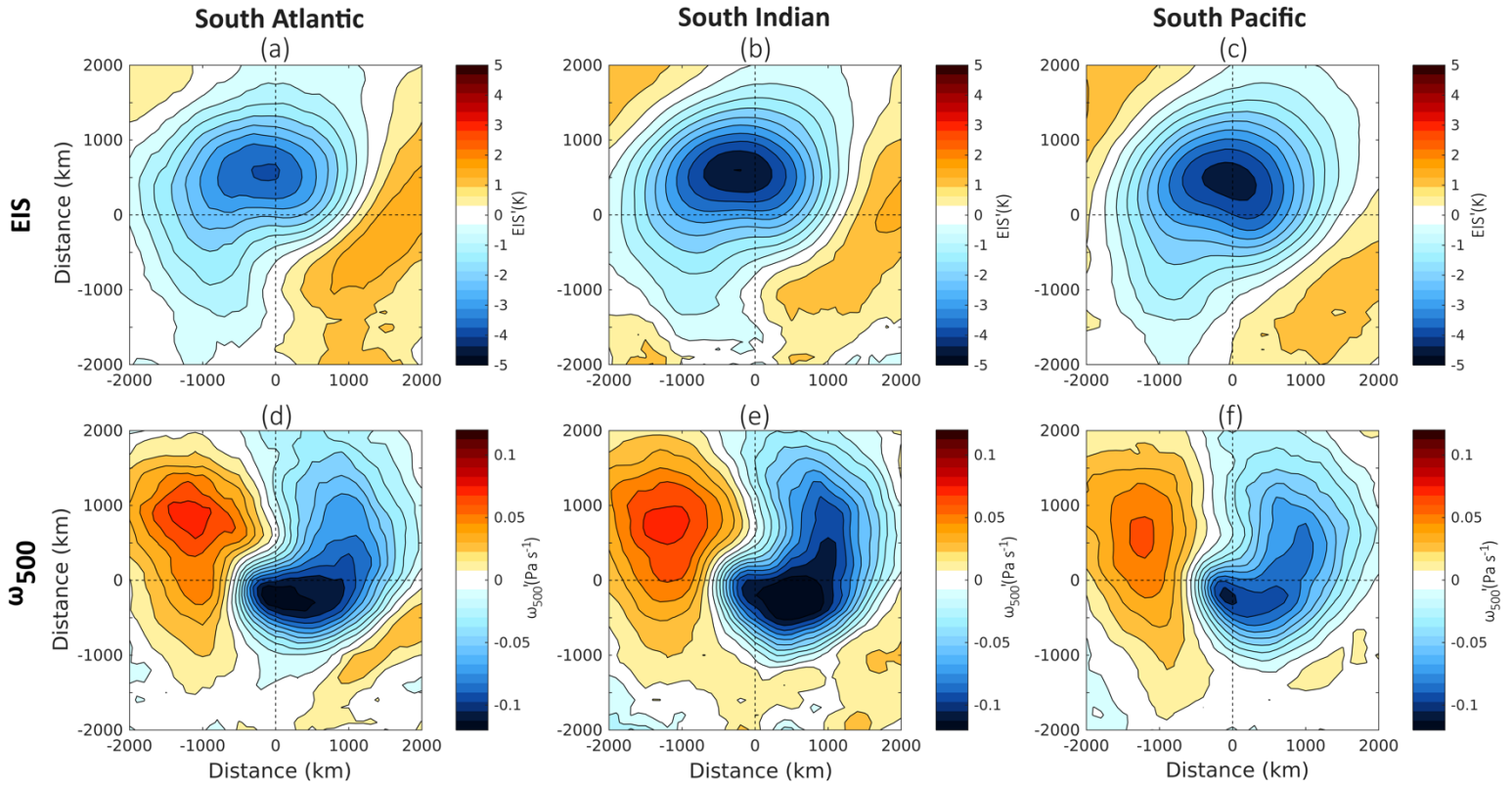
FIG. 9. Difference between the observed composite of daily SWCRE (W m^{-2}) around a Southern Ocean (45˚S–60˚S) extratropical cyclone during DJF and the corresponding cyclone composite for the HadGEM2-A model (HadGEM2-A - observations). Panel a retains the SWCRE climatology within both the observed and model cyclone composites, and panel b removes the SWCRE climatology from both the observed and model cyclone composites (as in Fig. 8c).

FIG. 10. Composites of the dynamical cloud controlling factors about a cyclone in three separate ocean basins where the top row represents composites of EIS and the bottom row represents composites in ω_{500}. The leftmost column contains the composites for the South Atlantic basin (70˚W-25˚E), the middle column contains the composites for the South Indian basin (25˚E-130˚E), and the rightmost column contains the composites for the South Pacific basin (130˚E-70˚W).
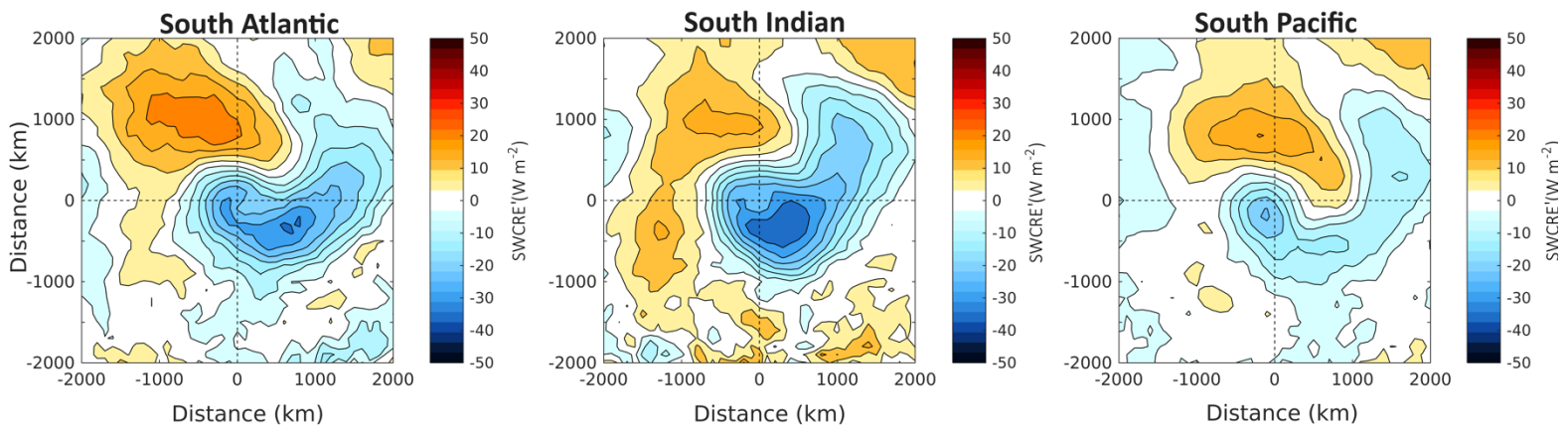
FIG. 11. Composites of shortwave CRE about a cyclone in three separate ocean basins. The basins cover the same ranges as in Fig. 10. The leftmost panel is for the South Atlantic basin, the middle panel is for the South Indian basin, and the rightmost panel is for the South Pacific basin.
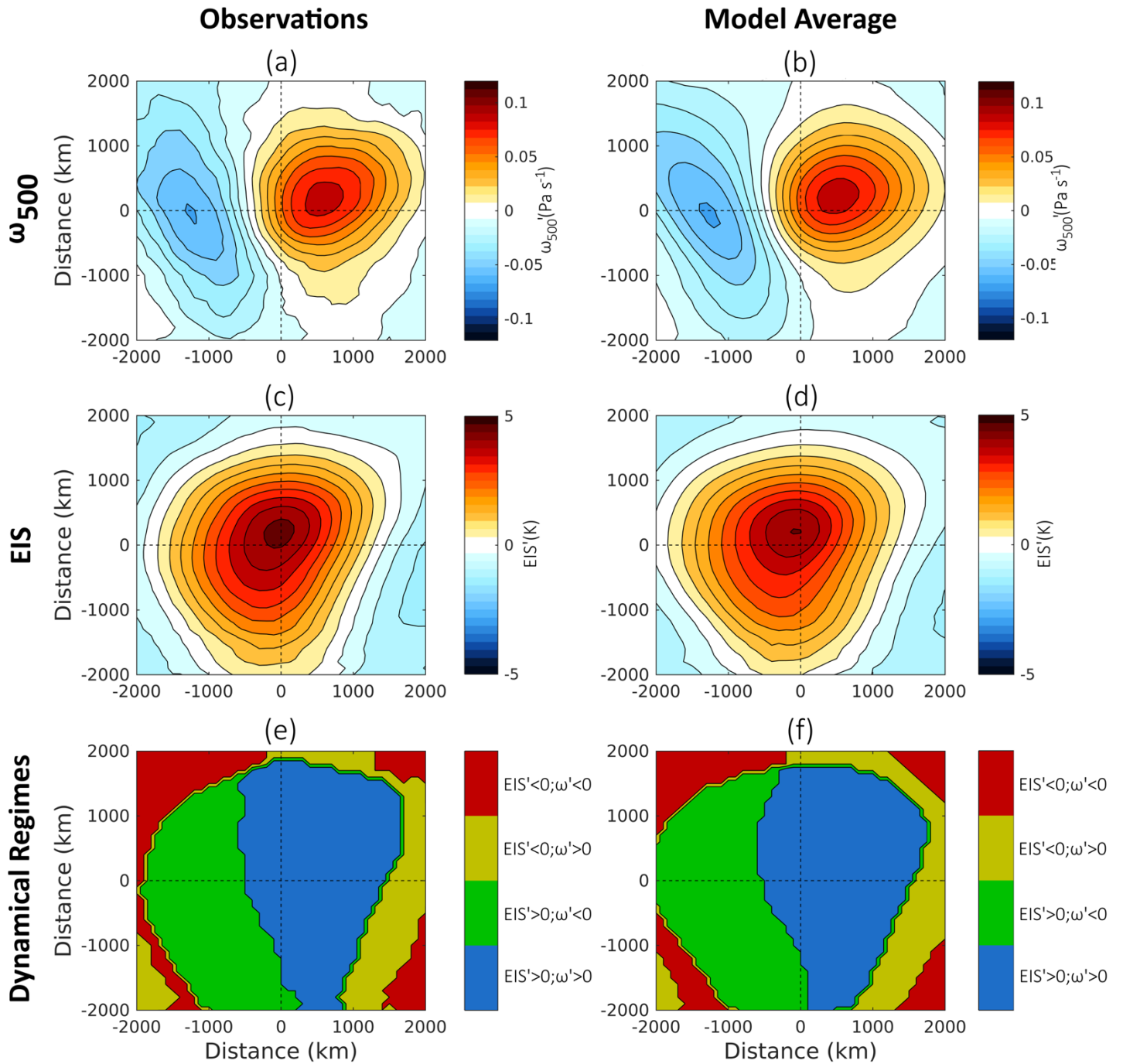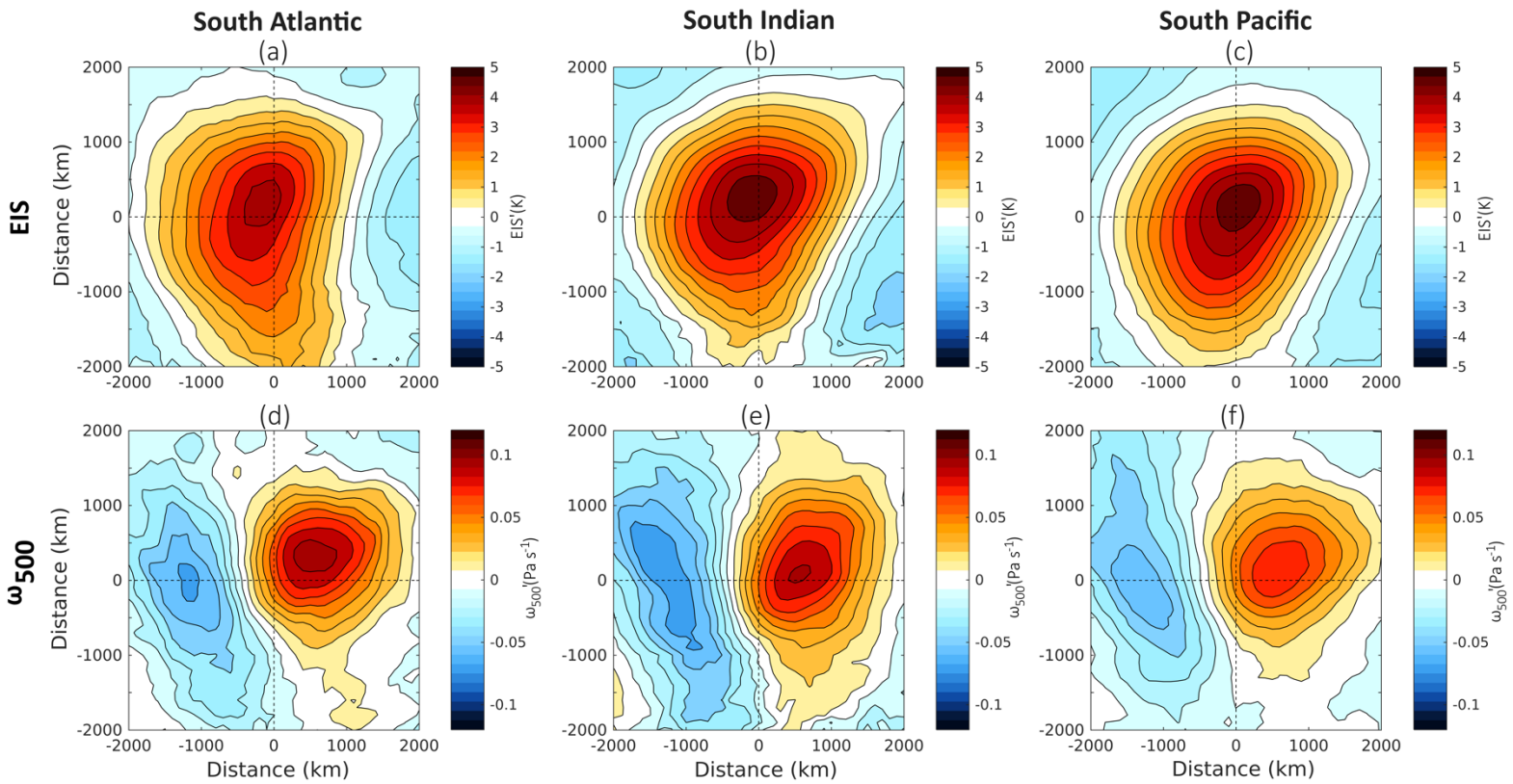
FIG. 12. As in Fig. 7, but for the cloud controlling factor composites around the centers of anticyclones over the Southern Ocean.
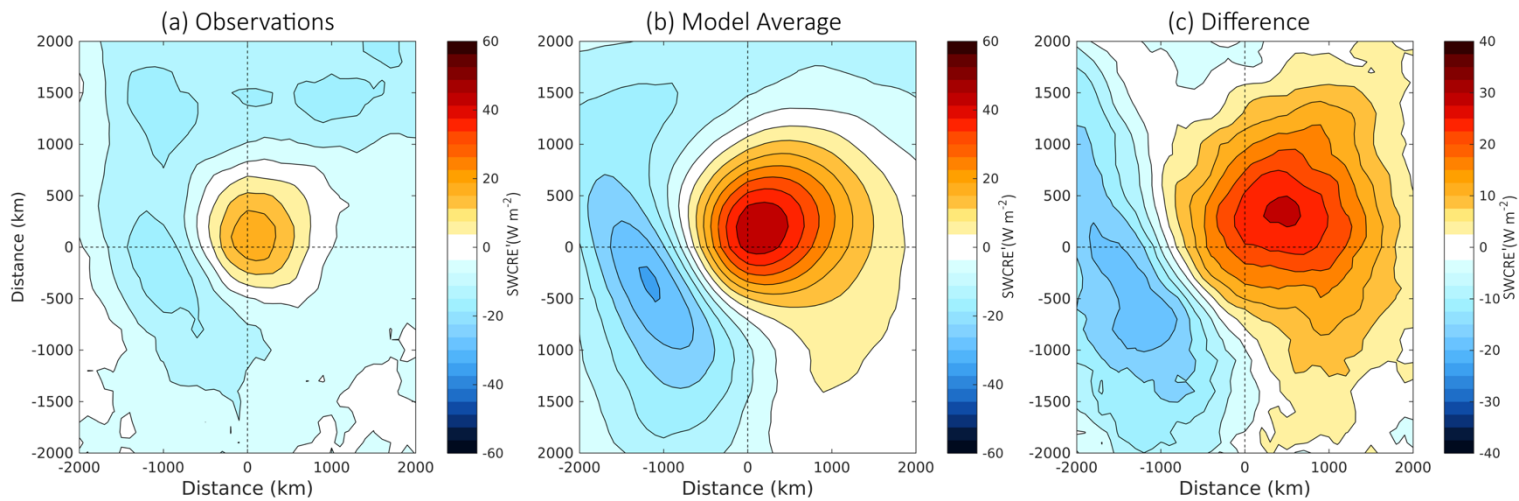
FIG. 13. As in Fig. 8, but for the SWCRE composites around the centers of anticyclones over the

Southern Ocean.

FIG. 14. As in Fig. 10, but for the cloud controlling factor composites around the centers of anticyclones over the different basins of the Southern Ocean.
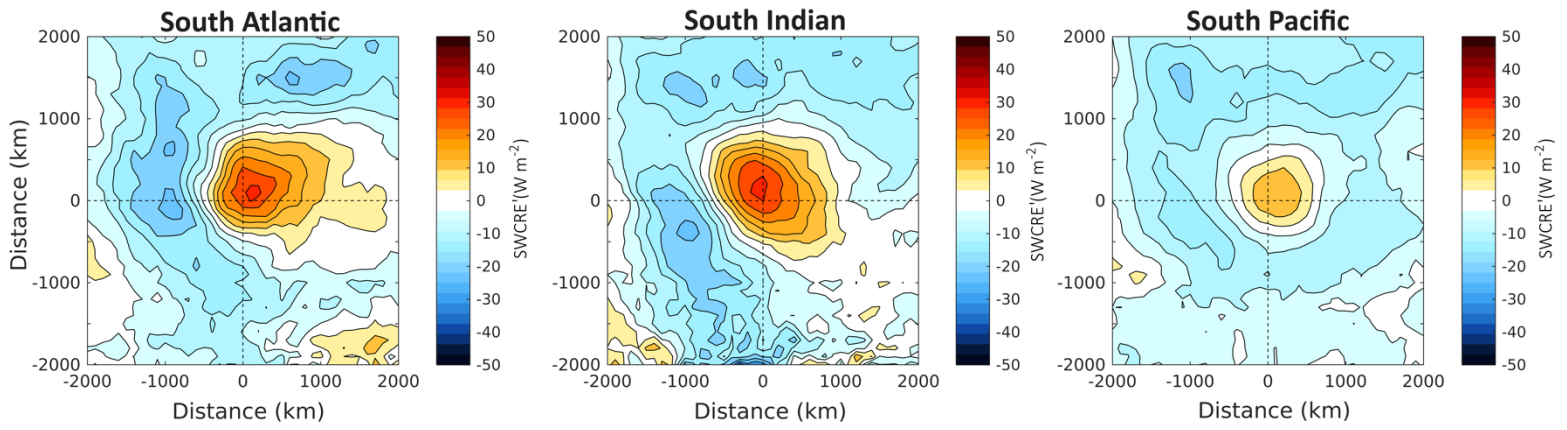
F<small>IG</small>. 15. As in Fig. 11, but for the shortwave CRE composites around the centers of anticyclones over the different basins of the Southern Ocean.
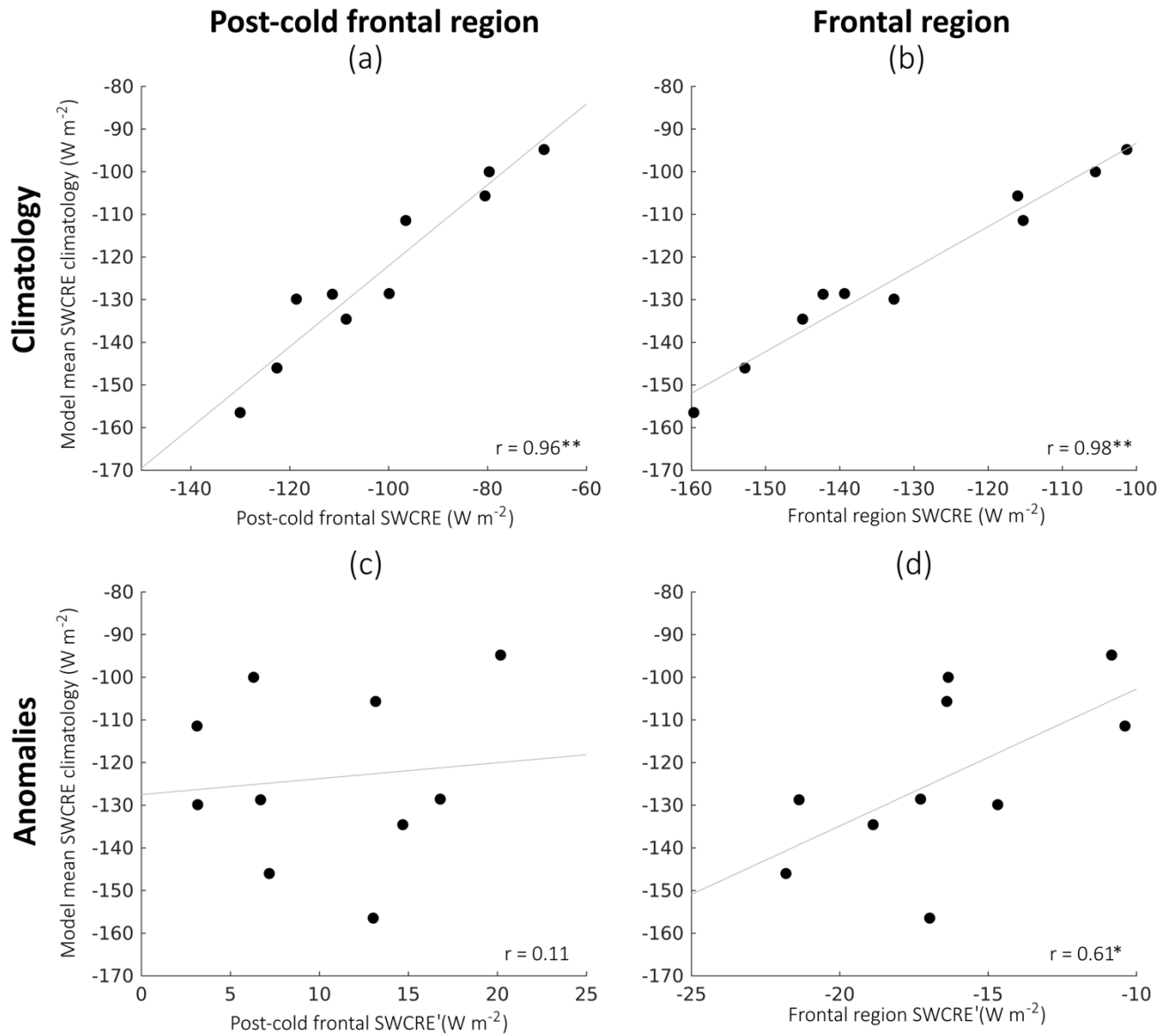
FIG. 16. Scatter plots relating the austral summer (DJF) SWCRE climatology (45˚S-60˚S) from

10 CMIP5 models to the: (a) model austral summer post-cold frontal region SWCRE

climatology (compare with Fig. 4 from Bodas-Salcedo et al. 2014), (b) model austral summer

frontal region SWCRE climatology, (c) model austral summer post-cold frontal region SWCRE

anomalies, and (d) model austral summer frontal region SWCRE anomalies. The post-cold

frontal and frontal regions are defined using the dynamical regimes shown in Fig. 7 (bottom,

yellow and red, respectively). The correlation coefficients for each scatter plot are shown in the

bottom right of each panel. Two asterisks denote significance at the 95% level or above, and one

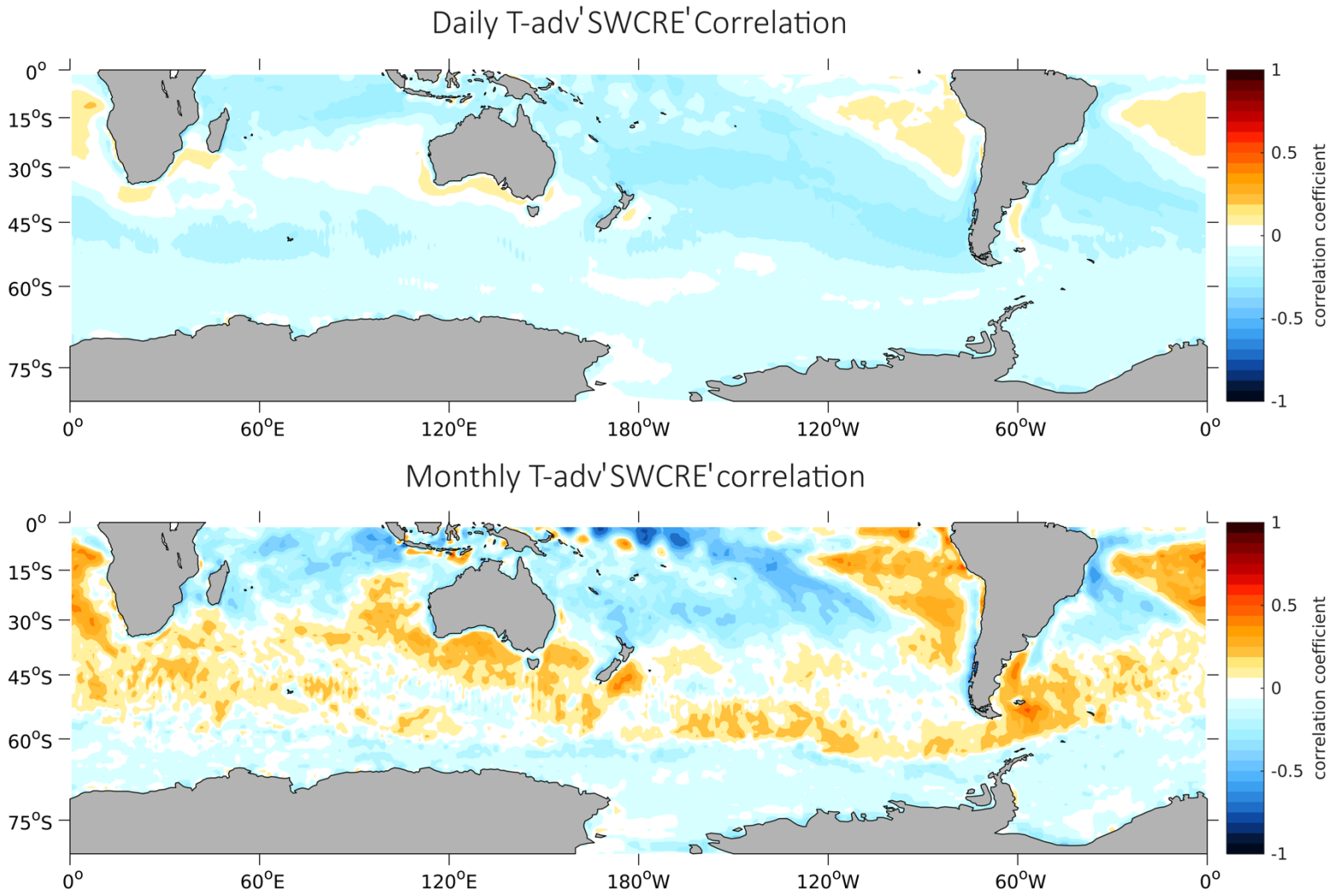asterisk denotes significance at the 90% level.

FIG. 17. Correlation coefficients between shortwave CRE anomalies and anomalies of surface thermal advection on a daily time scale (top) and a monthly time scale (bottom). Both correlations shown are for observations only.
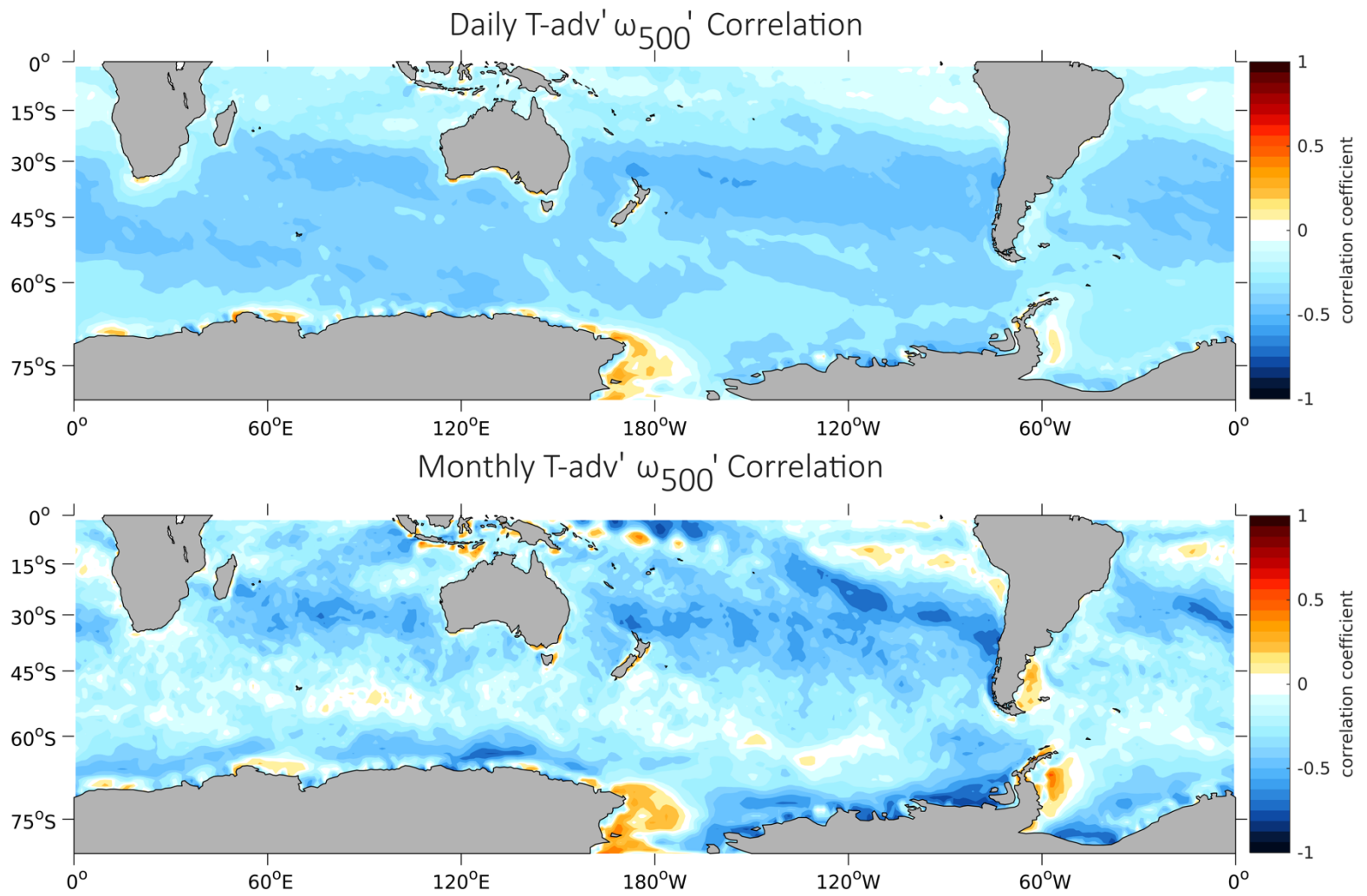
F𝙸G. 18. Correlation coefficients between surface thermal advection and ω_{500} on a daily time scale (top) and a monthly time scale (bottom). Both correlations shown are for the observations only.